v1.0 (Dec 2007)

The Milky Way Tomography with SDSS: III. Stellar Kinematics

Bond et al.

1. Data Description

An overview of SDSS imaging and spectrosopic surveys can be found in Papers I and II, and references therein. Briefly, SDSS imaging survey provides astrometry and *ugriz* photometry accurate to ∼0.02 mag for over 100 millions stars detected in close to 10,000 deg^2 of sky. These data can be used to estimate distance for main sequence stars, and metallicity for a subsample satisfying $0.2 < g-r < 0.6$ (F/G spectral types). Proper motion measurements based on a comparision of SDSS and POSS surveys are available for a subset of about 30 million stars. SDSS spectroscopic survey provides low-resolution spectra for close to 200,000 stars. These spectroscopic data are used to determine radial velocity for about 150,000 main-sequence stars, and also as a training sample for photometric metallicity estimator.

1.1. Photometric Parallax Relation

Summarize Paper I and refer to Sesar

Mention kinematic constraint and refer to later analysis

Point out correlation with metallicity from Paper II!

1.2. Photometric Metallicity Estimator

Summarize Paper II

1.3. The SDSS Radial Velocity Measurements

Take text from Prag and Serbia papers

1.4. The SDSS-POSS Proper Motion Measurements

We take proper motion measurements from the Munn et al. (2004) catalog, which is distributed as a part of public SDSS data release. This catalog is based on astrometric measurements from SDSS and a collection of Schmidt photographic surveys. Despite the sizable random and systematic astrometric errors in the Schmidt surveys, the combination of a long baseline (∼50 years for POSS-I survey), and a recalibration of the photographic data using positions of SDSS galaxies (see Munn et al. for details), results in median random proper motion errors of only ~ 3 mas yr^{-1} for $r < 18$ and ~ 5 mas yr^{-1} for $r < 20$ (per component). Systematic errors are typically an order of magnitude smaller, as robustly determined using spectroscopically confirmed SDSS quasars (see below). At a distance of 1 kpc, a random error of 3 mas yr^{-1} corresponds to a velocity error of ∼15 km/s, which is comparable to the radial velocity accuracy delivered by the SDSS stellar spectroscopic survey. At a distance of 7 kpc, a random error of 3 mas yr^{-1} corresponds to a velocity error of 100 km/s, which still represents a usable measurement for large samples, given that systematic errors are much smaller (∼20 km/s at a distance of 7 kpc).

Due to sufficiently small and well understood proper motion errors, together with a large distance limit (more than 100 times larger than for studies based on the Hipparcos survey, e.g. Dehnen & Binney 1998) and a large sample size (proper motion measurements are available for about 30 million stars from SDSS Data Relase 6), this catalog represents an unprecedently power resource for studying the kinematics of the Milky Way stars.

1.4.1. Determination of Proper Motion Errors Using Quasars

Quasars are sufficiently far away that their proper motions are negligible at the accuracy level considered here. The large number of spectroscopically confirmed SDSS quasars (Schneider et al. 2007), which were not used in the recalibration of POSS astrometry, can thus be used to derive robust independent estimates of, both random and systematic, proper motion errors. The distributions of proper motions for 54,811 quasars with $15 < r < 20$ have a standard deviation of ∼3.5 mas/yr for each component (determined from inter-quartile range), with medians differing from zero by less than 0.2 mas/yr. The standard deviation, which represents a measurement of random errors, is a function of apparent magnitude, and well summarized by the following empirical fit

$$\sigma_\mu = 2.7 + 2.0\,10^{0.4\,(r-20)}\,\mathrm{mas/yr} \tag{1}$$

in the $15 < r < 20$ range. When the measurements of each proper motion component are normalized by σ_μ, the resulting distribution is essentially Gaussian, with only ∼1.4% of the sample deviating by more than 3 from zero. The correlation between the two components is negligible compared to the intrinsic scatter.

The median proper motions for the full quasar sample show that the systematic errors averaged over the whole observed sky region are at most 0.2 mas/yr. However, they can be larger by a factor of 2-3 in small sky patches, as illustrated in Figure 1. We find that the distribution of systematic proper motion errors in ~100 deg^2 large patches has a width of ~0.67 mas/yr (same for each component), or about twice as large as expected from purely statistical noise (per bin). As the figure shows, a few regions of the sky have coherent systematic errors at the level close to 1 mas/yr (e.g. the median μ_l towards $l \sim 270°$, or μ_b towards the inner Galaxy). Therefore, the interpretation of kinematics measured using proper motions towards these regions should be cautious.

The region with the largest systematic errors, $\sim$ 1 mas/yr for μ_l (the top region in the top left panel in Figure 1), is observed at low declination ($\delta \lesssim 10°$). The systematic deviation of quasar vector proper motions from zero is approximately parallel to the lines of constant right ascension ($\langle\mu_\alpha\rangle \sim 0$, and $\langle\mu_\delta\rangle \sim -1$ mas/yr), which suggests that this effect could be caused by atmospheric refraction (due to spectral differences between quasars and galaxies used in the recalibration of POSS astrometry). Such an effect would be the strongest for observations obtained at high airmass, which increases for fields with low declinations (the POSS data were obtained at a latitude of +33°; the SDSS database does not include the airmass information). We find that the median quasar proper motion in the δ direction is well described by

$$\langle\mu_\delta\rangle = -0.72 + 0.019\,\delta \ \ \text{mas/yr} \tag{2}$$

for $-5° < \delta < 30°$, and $\langle\mu_\delta\rangle \lesssim 0.2$ mas/yr for $\delta > 30°$.

The observed direction and the magnitude of this systematic offset (an astrometric displacement of up ~30 mas) are consistent with detailed studies of atmospheric dispersion effects for quasars (Kaczmarczik et al. 2008). Therefore, it is possible that true systematic errors for stellar proper motions (whose spectral energy distributions differ less from galaxy spectral energy distributions than is the case for quasars) are smaller than implied by Figure 1. Nevertheless, we will conservatively adopt results based on quasars as independent estimates of systematic and random proper motion errors for stars analyzed in this work. In particular, we adopt 0.67 mas/yr as an estimate for typical systematic proper motion error.

A proper motion of 0.67 mas/yr corresponds to 3 km/s at 1 kpc and ~20 km/s at 6 kpc. At the same time, systematic distance errors are responsible for a ~10% systematic velocity uncertainty. Hence, proper motion systematics dominate at distances beyond 1 kpc for a heliocentric tangential velocity of 30 km/s, at at distances beyond 6 kpc for a heliocentric tangential velocity of 200 km/s. It turns out that throughout most of the

Galaxy volume analyzed in this work, the systematic distance errors are more important effect than systematic proper motion errors (though the latter display a coherent behavior as a function of position on the sky in certain directions).

The quasar sample has a much narrower color distribution than main sequence stars (96% of quasar sample satisfies $-0.2 < g-r < 0.6$), and provides a better estimate of systematic proper motion errors for blue than for red stars. Within the $-0.2 < g-r < 0.6$ color range, we find that the gradient of median proper motion is $\lesssim 0.1$ mas/yr/mag (per component). When the fit is extended to $g-r < 1.6$ (using a much smaller number of quasars), the gradient is still smaller than 0.5 mas/yr/mag. Hence, the color systematics are smaller than, or at most comparable to, proper motion systematics as a function of position on the sky.

In addition to their dependence on magnitude, the random proper motion errors also depend on the position on the sky, but the variation is much smaller than for systematic errors (see right panels in Figure 1). A region with the largest deviation ($170^\circ < \alpha < 230^\circ$ and $\delta < 10^\circ$, corresponding to $300^\circ < l < 330^\circ$) has the distribution width for the proper motion component parallel to right ascension increased to 5 mas/yr, from 3-4 mas/yr for the rest of the sky (and for the other component).

1.5. Complexities Associated with Kinematic Analysis

Analysis of stellar kinematics presented here is significantly more complex than analysis presented in the first two papers. In Paper I we discussed the variation of stellar counts, a scalar quantity, as a function of position in the Galaxy. In Paper II we presented an analogous analysis of metallicity distribution – an added complexity compared to Paper I because the quantity of interest is a distribution function rather than a scalar. Here we analyze a distribution function for a vector quantity, the three-dimensional velocity, which not only has three components, but they can be correlated in a complex way. Even for a perfect Gaussian velocity distribution, there are still as many as nine scalar functions to follow as a function of position in the Galaxy and metallicity. Another way to look at the same problem, more similar to analysis presented in Paper I, is that we are trying to count stars and constrain the distribution function in the 7-dimensional space spanned by three spatial coordinates, three velocity components and metallicity. Assuming rotational symmetry and that stars can be simply separated in low-metallicity and high-metallicity subsamples, this is still counting in a 5-dimensional space.

An added difficulty when analyzing kinematics is complex error behavior. Random errors for radial velocity measurements depend on magnitude, and thus distance, due to varying signal-to-noise ratio. When using proper motions, in addition to a strong dependence of random velocity errors on distance, systematic errors are also a function of position on the sky. When radial velocity and proper motion measurements are analyzed simultaneously, the various systematic and random errors combine in a complex way and substantial care is needed when interpreting results. Due to this fact, the presentation of our analysis is much more involved than would be a case for a dataset with much smaller, or less complex, errors. Nevertheless, this dataset represents a major step forward in exploration of the Galaxy due to its large size, large distance limits, and sufficiently small errors to resolve some major features in the kinematic behavior of the Milky Way stars.

1.6. Coordinate Systems and Velocity Corrections

Take text from Paper II and earlier writeup

We correct velocities for solar motion relative to the local standard of rest using values based on the Hipparcos survey ($v_X^{\odot} = -10.0 \pm 0.4$ km/s, $v_Y^{\odot} = -5.3 \pm 0.6$ km/s; and $v_Z^{\odot} = 7.2 \pm 0.4$ km/s; Dehnen & Binney 1998). For the rotational velocity of the local standard of rest, we adopt $v_{LSR} \sim 220$ km/s (Gunn, Knapp & Tremaine 1979). The sensitivity of our results to these values is discussed below.

1.7. The Three Main Subsamples

To facilitate initial analysis of these new voluminous data sets, as well as to simplify presentation, we separate stars in three subsamples.

Describe $0.2 < g-r < 0.4$ F/G subsample of disk and halo stars, and the red subsample.

2. Analysis of Proper Motion Sample

We begin by analyzing proper motion measurements for stars observed towards the North Galactic pole ($b > 80$). Towards this region, the azimuthal velocity component, v_Φ, and the radial velocity component, v_R, can be determined with sufficient accuracy from the proper motion measurements alone (i.e. without knowing the radial velocity, v_{rad}). This analysis yields significant insight in the kinematic behavior as a function of metallicity and distance from the galactic plane, Z. We then extend this analysis to the whole meridional

$Y = 0$ plane and study the variation of kinematics as a function of both R and Z. In this section we only consider the northern Galactic hemisphere, where most of the proper motion data is available. We analyze both hemispheres in the next Section, when discussing the radial velocity measurements.

2.1. Analysis of Proper Motions towards the North Galactic pole

We have shown in Paper II that disk and halo stars can be efficiently and robustly separated using photometric metallicity boundary $[Fe/H] = -1$. As already indicated in Paper II, they also display remarkably different kinematic behavior. While this conclusion is qualitatively the same as discussed in the seminal paper by Eggen, Lynden-Bell & Sandage (1962), the new data analyzed here and in the companion papers allow us to extend their result beyond the solar neighborhood and reproduce it *in situ* with a ~100 times larger sample.

Here comes a 3-panel figure with a) the bottom right panel from Fig. 8 in Paper II, b) counts vs. Z with separate components and J08 fit (don't forget to look at the full sample, not only pm), and c) binned median vPhi (corrected for LST and the Sun)

The differences are not only in the medians but the whole distributions: ivezicFig4.eps (but vertical) from Shanghai paper to demonstrate that the differences are real effect

Figure **??** summarizes the differences in the behavior of azimuthal velocity component between halo and disk stars. Comment on dispersion.

Analogous figure for the radial component. Is this a local effect, errors in proper motions? Refer to section on meridional plane for further analysis.

2.1.1. The Vertical Shear of the Azimuthal Velocity Component

The most interesting result for disk stars is the velocity shear List earlier refs (or postpose for discussion?)

Here compare for color bins for red stars and demonstrate that the shear is non-linear, Figure 9

2.1.2. The Negative Radial Velocity Component

The most confusing result for disk stars is the negative gradient of the radial velocity component with Z.

The right column in Figure 9

Figure with color-coded median pm:

Also, refer to 6D sample which shows the same effect for $Z < 0$

2.1.3. The v_Φ vs. v_R Correlation and Velocity Substructure

Refer back to figure ivezicFig4.eps mentioned above

Demonstrate that v_Φ vs. v_R correlation is real

Show that halo feature is localized Look at FINDME in analyzePM.macro Dont forget -0.9 and -1.1 instead of -1.0

Show 3 slices for red stars (ivezicFig3.eps from Shanghai paper)

If there were no spatial variation of the velocity distribution function and $\langle v_Z \rangle = 0$, then v_X measures v_R

2.2. Analysis of Proper Motions in the Meridional $Y \sim 0$ Plane

Under the assumption that the median of vertical velocity component, v_Z, is zero, supported by analysis presented in Section 3, the measurement of latitudinal proper motion, μ_b, still provides a good constraint for the behavior of the radial velocity component, v_R.

We first presented the global behavior, as traced by median and dispersion, and now we show projections of the full velocity distribution function.

Point out similarities with the Hipparcos results at small Z.

Main question: is v_Φ - v_R correlation data artefact, or real? The lines of constant (and non-zero) pmY are aligned with D=const. This is unlikely to be a coincidence! This can be shown by making two r vs g-i CMDs like e.g. the top two in

3. Analysis of Radial Velocity Sample

Although much smaller sample, and susceptible to selection effects, allows to study all nine components of the velocity ellipsoid, and as a function of R and Z, to a distance of $\lesssim$ 10 kpc.

Table 1. The median velocity and velocity dispersion

$[Fe/H]$	R (kpc)	Z (kpc)	N^a	$\langle v_\Phi \rangle$	$\langle v_R \rangle$	σ_Φ	σ_{RZ}	σ_{obs}^b	σ_Φ^{corr}	σ_{RZ}^{corr}	σ_R^0
< -1.1	5–6.5	3–4	6487	-90	-57	104	105	60	85	86	105
< -1.1	7–9	3–4	4979	-66	-46	96	112	49	84	101	101
< -1.1	10–12	3–4	3375	-38	-23	89	59	52	72	28	37
> -0.9	10–12	3–4	1548	-134	-21	91	68	50	76	46	62

[a]The number of stars selected by the listed metallicity, R and Z selection criteria. The distributions of the measured v_Φ and v_{RZ}, together with best Gaussian fits listed here, are shown in Figure 16. See text for the definitions of v_{RZ} and σ_{RZ}.

[a]The median velocity measurement error (km/s) derived from proper motion errors. This error estimate is used to compute implied intrinsic velocity dispersion for each velocity component, listed in the last three columns. The σ_R^0 listed in the last column is computed from σ_{RZ}^{corr} using the v_Z=0 ansatz.

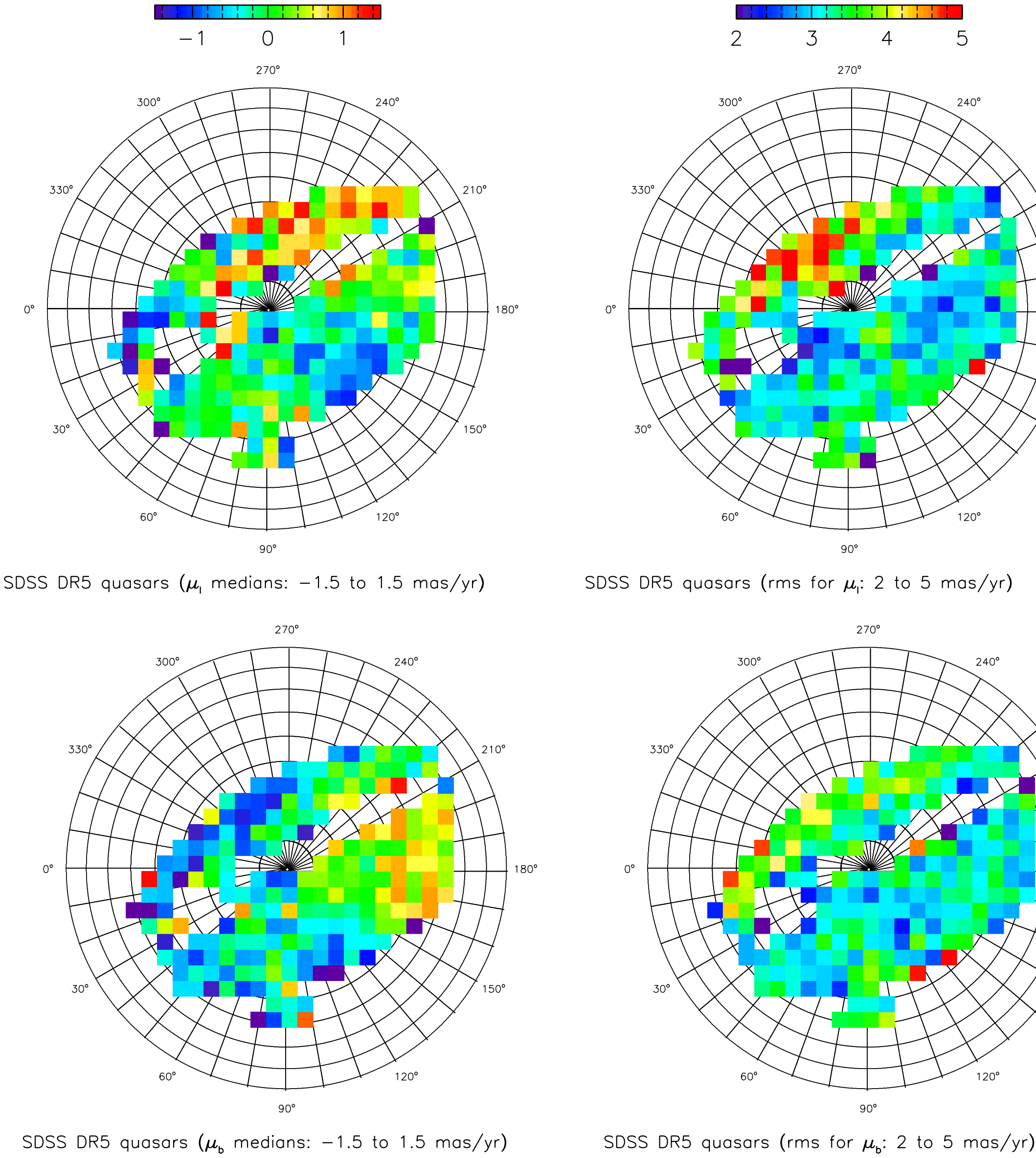

Fig. 1.— An estimate of systematic and random proper motion errors in the Munn et al. (2004) SDSS-POSS catalog, as a function of position on the sky, determined using a large sample of spectroscopically confirmed SDSS quasars. The top left and bottom left panels show the median proper motions for 45,348 quasars with $15 < r < 20$ and $b > 0°$, evaluated in approximately 100 deg^2 large bins, and displayed in Lambert projection (top: μ_l, bottom: μ_b). The color coding is linear in the range -1.5 mas/yr to 1.5 mas/yr, as shown in the legend on top. The median statistical noise per pixel is ∼0.3 mas/yr. The distribution width for these medians (rms), indicative of systematic proper motion errors, is ∼0.67 mas/yr for each component, or about twice as large as expected from purely statistical noise. The top and bottom right panels show the the root-mean-scatter for each bin (top: μ_l, bottom: μ_b), displayed on a linear scale from 2 mas/yr to 5 mas/yr (the scatter for individual measurements depends on magnitude, see text). Note coherent behavior for some sky regions.

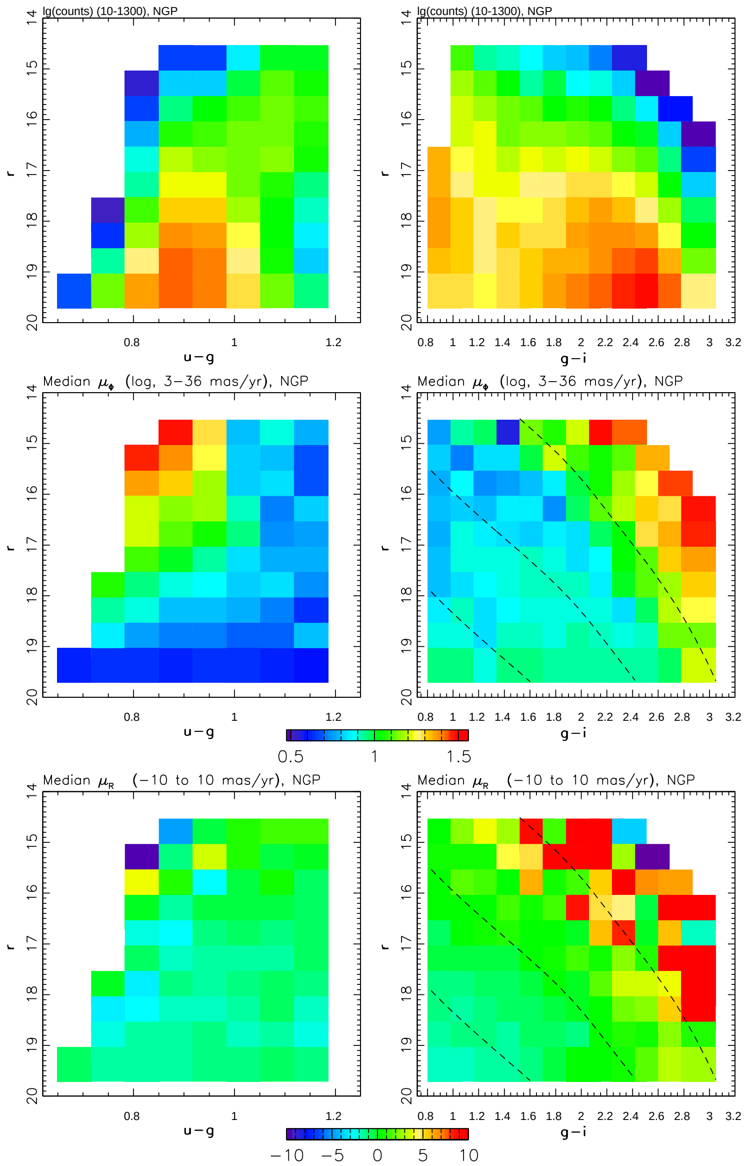

Fig. 2.— The counts (top) and the median proper motion in the azimuthal (middle) and radial directions (bottom) for stars towards the North Galactic pole ($b > 80°$). The r vs. $u-g$ color-magnitude diagrams in the left column are produced with $\sim 64,000$ F/G main-sequence stars selected by $0.2 < g-r < 0.4$. For these stars, the $u-g$ color measures metallicity, and $u-g = 1.0$ approximately corresponds to $[Fe/H] = -1.0$. For a given r, the distances are roughly constant due to the narrow selected $g-r$ range. Note the clear separation of halo ($u-g < 1$) and disk ($u-g > 1$) stars in the top left panel, and the abrupt change of the median azimuthal proper motion at this boundary in the middle left panel. The r vs. $g-i$ color-magnitude diagrams in the right column are produced with $\sim 200,000$ main-sequence G/K/M stars selected by $g-i > 0.8$ (roughly $g-r > 0.6$). For these stars, the absolute magnitude is a strong function of the $g-i$ color, and the location of distances equal to 300 pc, 1 kpc and 3 kpc are shown by the dashed lines in the middle and bottom left panels.

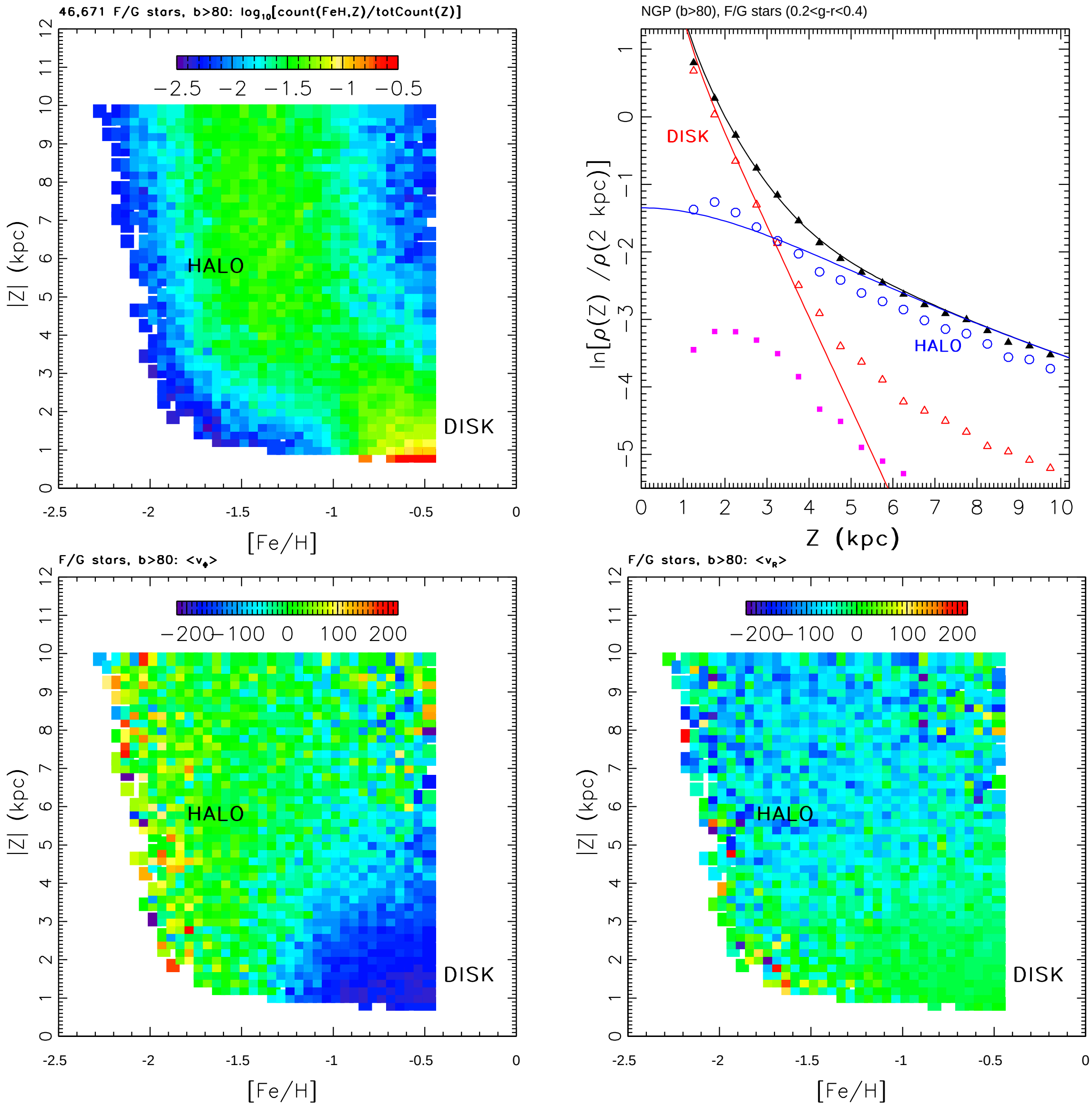

Fig. 3.— The top left panel shows the metallicity distribution at a given distance from the Galactic plane for ∼47,000 stars observed towards the North Galactic pole ($b > 80°$), with $0.2 < g - r < 0.4$ and good proper motion measurements. The conditional probability density for a given Z is shown on a logarithmic scale (with the color legend shown in the panel), with its integral normalized to 1. The two concentrations of stars correspond to disk ($[Fe/H] \sim -0.7$) and halo ($[Fe/H] \sim -1.5$) stars, as marked in the panel. The counts for these two subsamples, separated by $[Fe/H] = -1$, are shown in the two right panel as open triangles and circles, respectively. Their sum is shown as solid triangles, with the the best-fit model from Paper I shown by lines. The solid squares show the counts for a subsample of stars identified using kinematic measurements (see text). The bottom two panels show the medians for the azimuthal (v_Φ, left) and radial (v_R, right) velocity components, with the color legend (in km/s) shown in each panel. Note the remarkable difference in the v_Φ distributions between halo and disk stars.

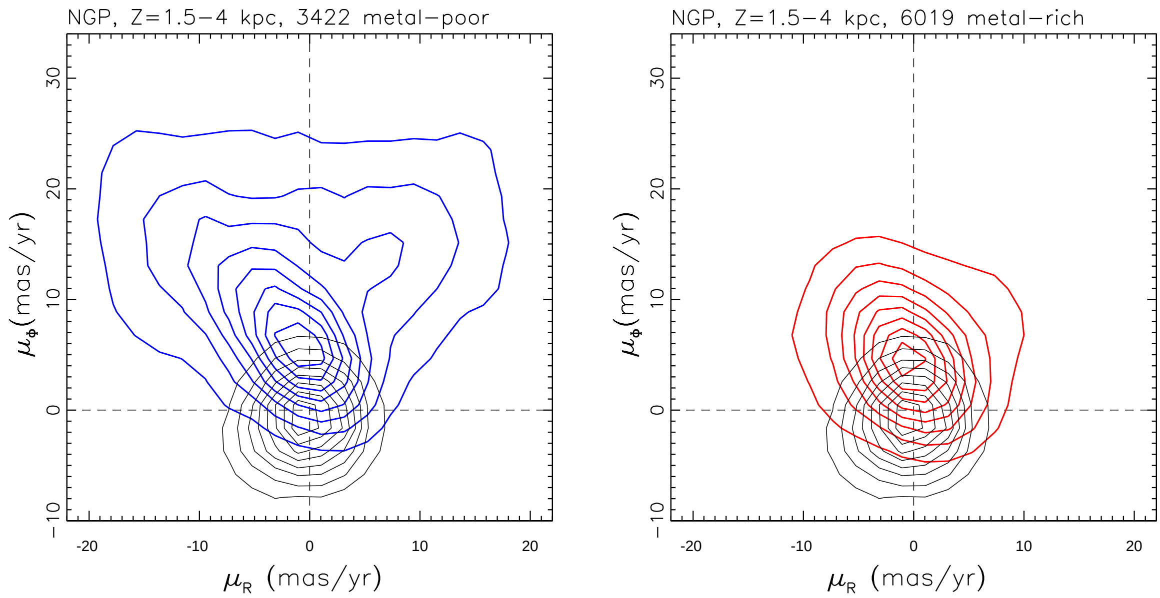

Fig. 4.— Proper motion distributions for two subsamples of F/G stars, selected by $0.2 < g - r < 0.4$, observed towards the North Galactic pole ($b > 80°$), and at distances 1.5–4 kpc above the plane. The proper motion component towards $l = 180°$ is shown on the x axis (μ_R), and the component towards $l = 270°$ is shown on the y axis (μ_Φ). The proper motion distribution for high-metallicity (disk) stars ($[Fe/H] > -1$) is shown in the left panel, and for low-metallicity (halo) stars in the right panel. In each panel, the thin contours centered on the origin show the proper motion distribution for 498 spectroscopically confirmed quasars with $b > 80$. Note that the <1 mas/yr systematic proper motion errors illustrated in Figure 1 are barely visible in this plot.

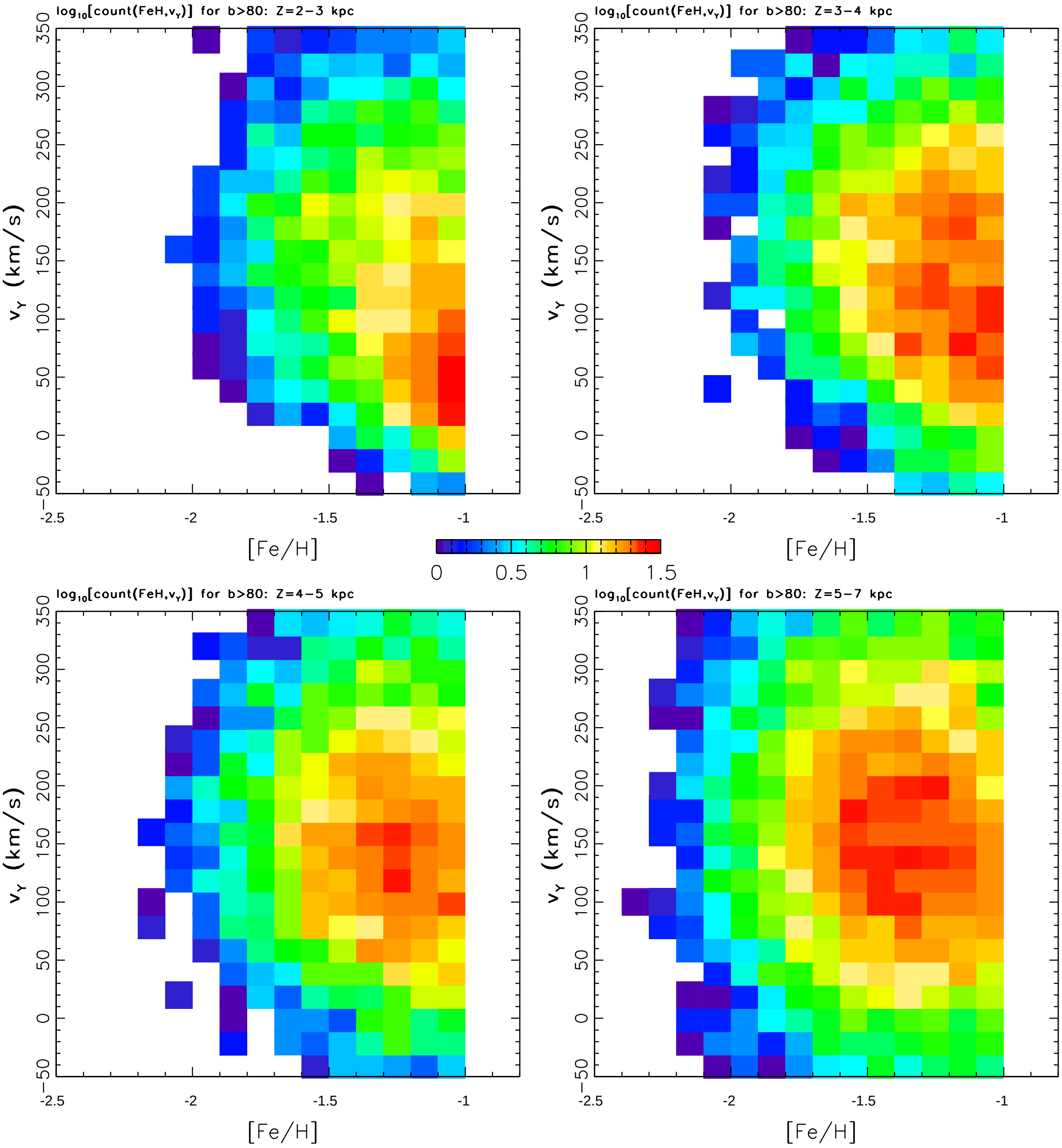

Fig. 5.— The distribution of stars with $[Fe/H] < -1$ observed towards the north Galactic pole ($|b| > 80°$) in the velocity-metallicity diagrams, and as a function of distance from the plane in the range 2–7 kpc (top left: 2–3 kpc, 6458 stars; top right: 3–4 kpc, 7558 stars; bottom left: 4–5 kpc, 8046 stars; bottom right: 5–7 kpc, 14591 stars). The y axis is the heliocentric velocity component in the Y direction (opposite to the direction of galactic rotation). The color map shows counts on a logarithmic scale illustrated in the middle of the figure. The top left panel is dominated by disk stars with $[Fe/H] \sim -1$ and $v_Y \sim 50$ km/s, at the two bottom panels are dominated by halo stars with $[Fe/H] \sim -1.4$ and $v_Y \sim 150$. In the bottom right panel, the gradient $dv_Y/d[Fe/H]$ of -6 km/s/dex is consistent with zero.

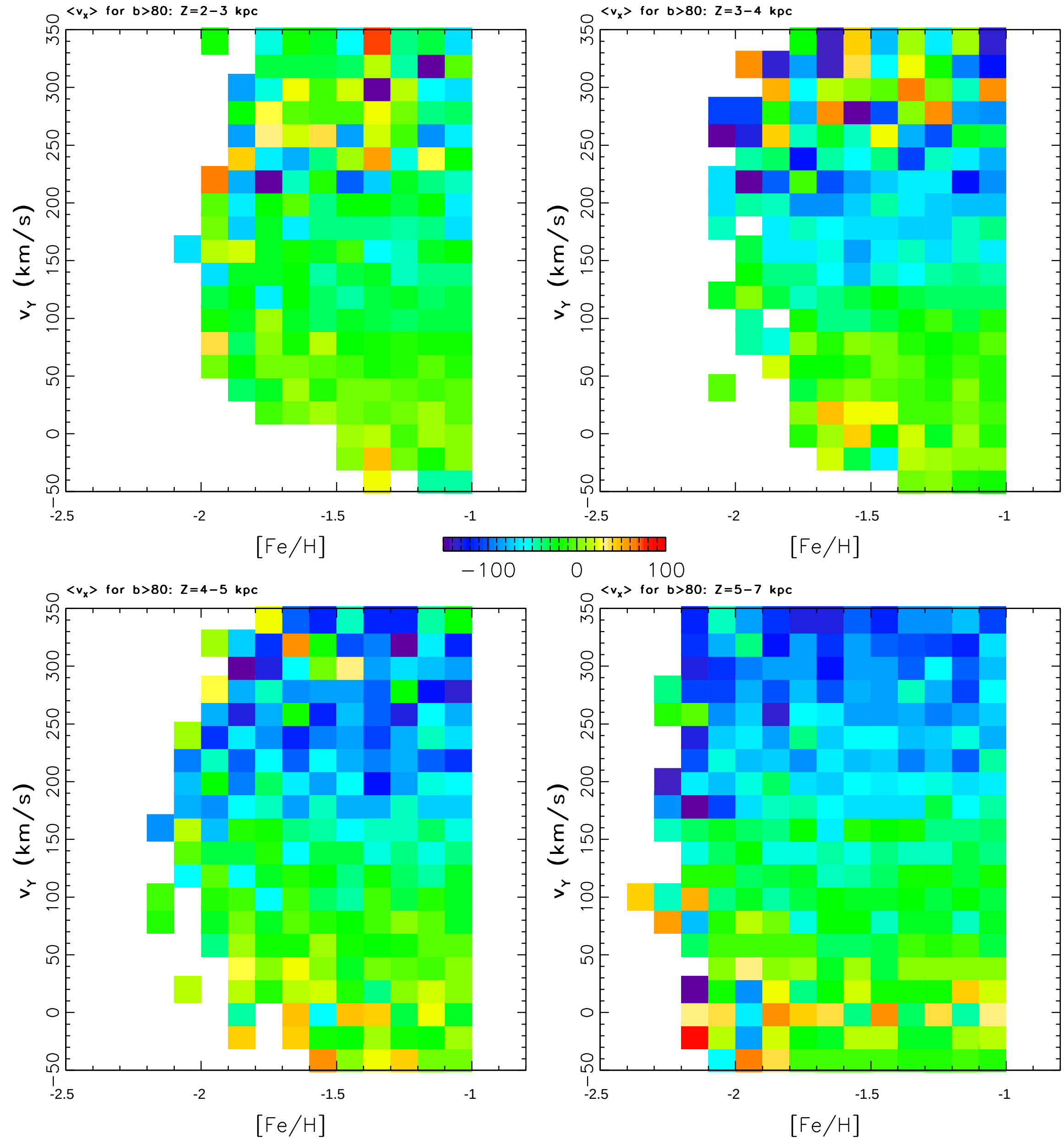

Fig. 6.— Analogous to Figure 5, except that the median heliocentric velocity component in the X direction (towards galactic anti-center) is shown instead of counts, on a linear scale illustrated in the middle of the figure (km/s). Note the strong correlation between v_X and v_Y, and a lack of v_X dependence on metallicity, for Z bins dominated by halo stars. Note also that $\langle v_X \rangle$ is negative (motion towards the galactic center) for $v_Y > 150$ km/s.

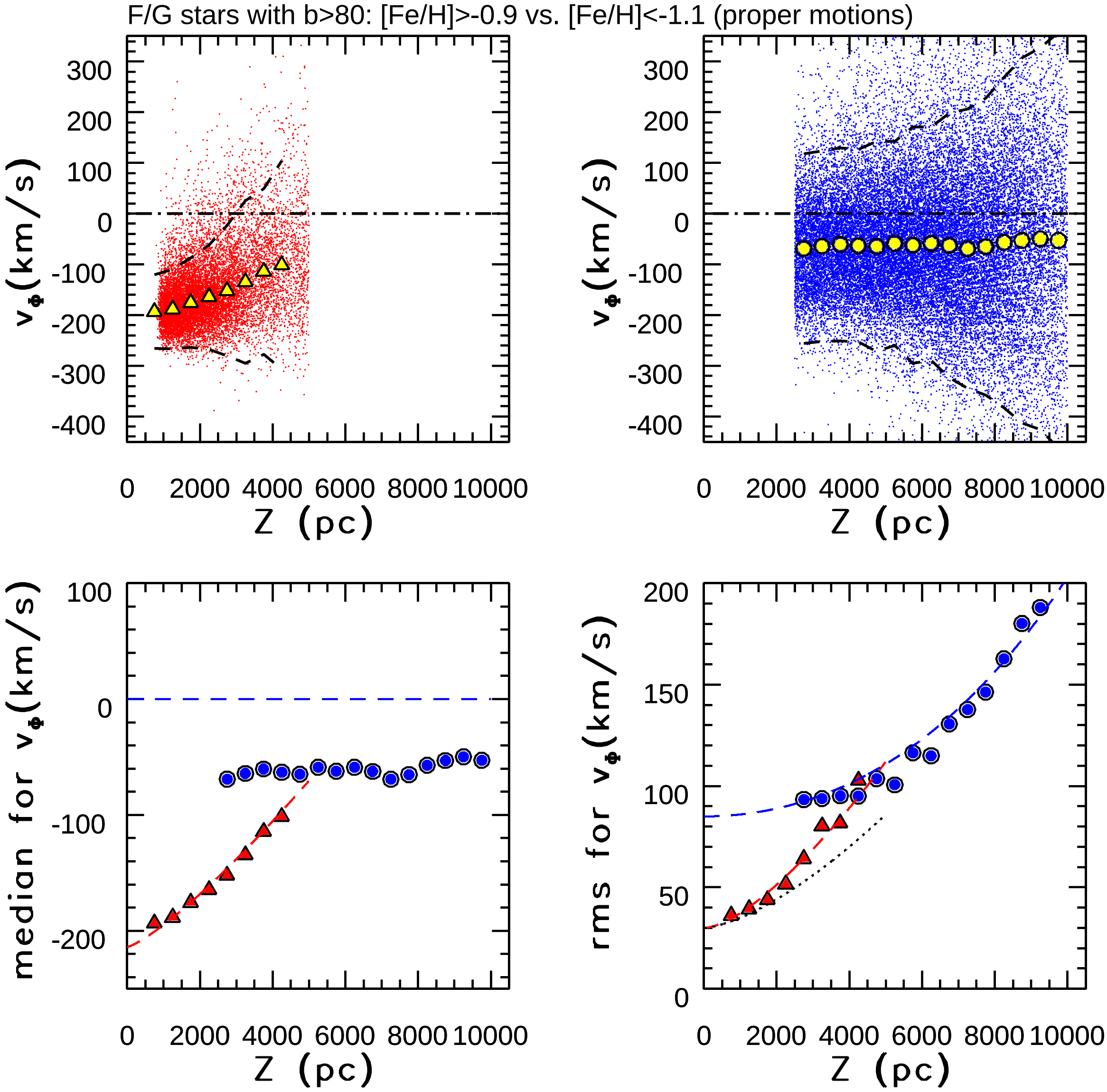

Fig. 7.— The dots in the top two panels show the azimuthal velocity component, v_Φ, as a function of the distance from the plane, Z, for ~11,000 high-metallicity (left, $[Fe/H] > -0.9$) and ~14,000 low-metallicity (right, $[Fe/H] < -1.1$) stars detected towards the North Galactic pole ($b > 80$). For each subsample, the Z range where contamination from other subsample is non-negligible is excluded. The large symbols show the median values, and the 2σ envelope around the medians is shown by dashed lines. The bottom two panels compare the medians (left) and velocity dispersion (right) for the two subsamples shown in the top two panels. The lower dashed line in the bottom left panel is an empirical fit to the velocity shear profile. The two dashed lines in the bottom right panel are analogous fits for the velocity dispersion, with measurement errors taken into account. The intrinsic velocity dispersion for low-metallicity stars is assumed constant, and the dotted line shows the intrinsic velocity dispersion for high-metallicity stars.

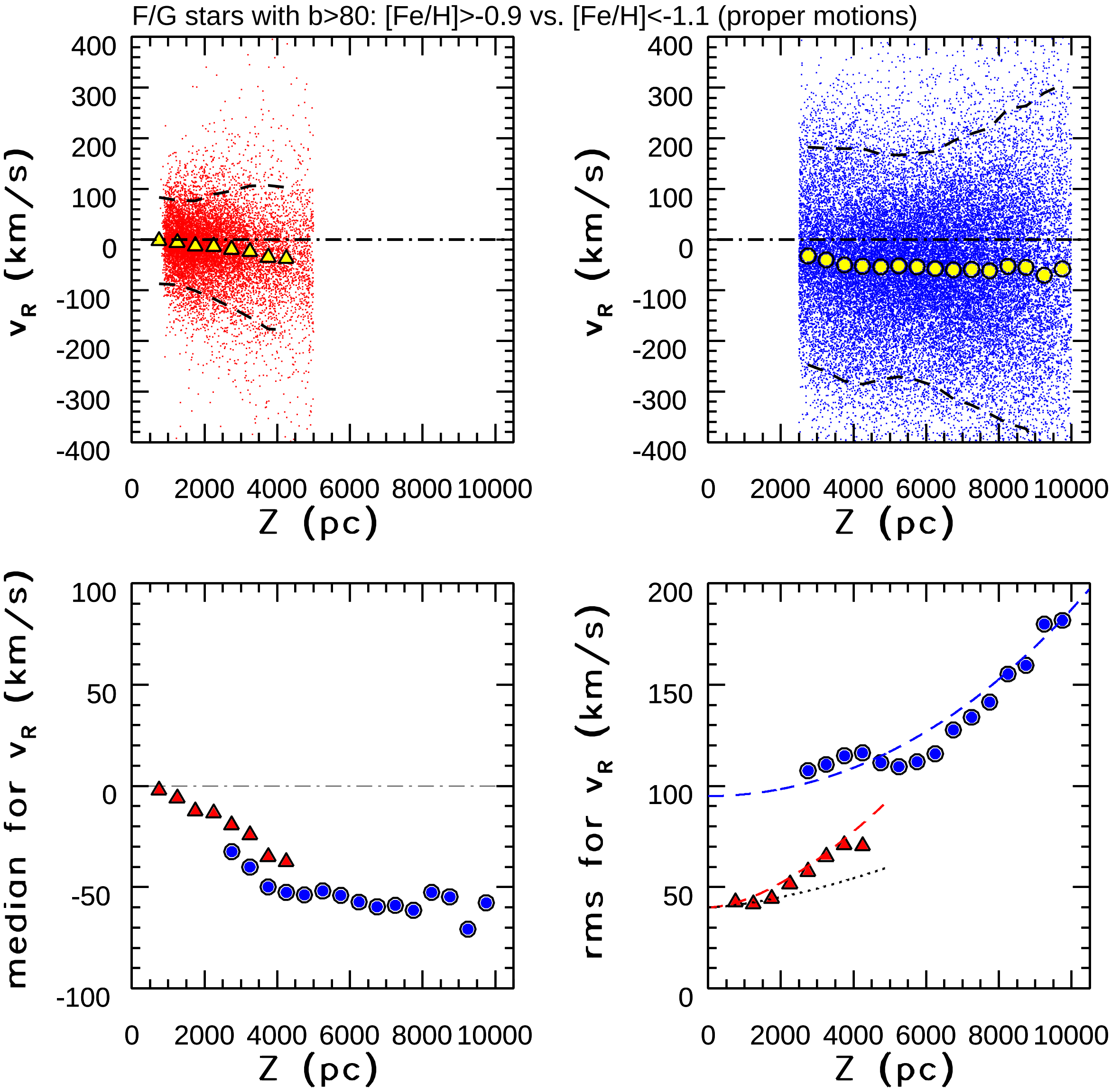

Fig. 8.— Analogous to Figure 7, except for the radial velocity component, v_R. Note that the median v_R deviates from zero at large Z for both subsamples (bottom left panel).

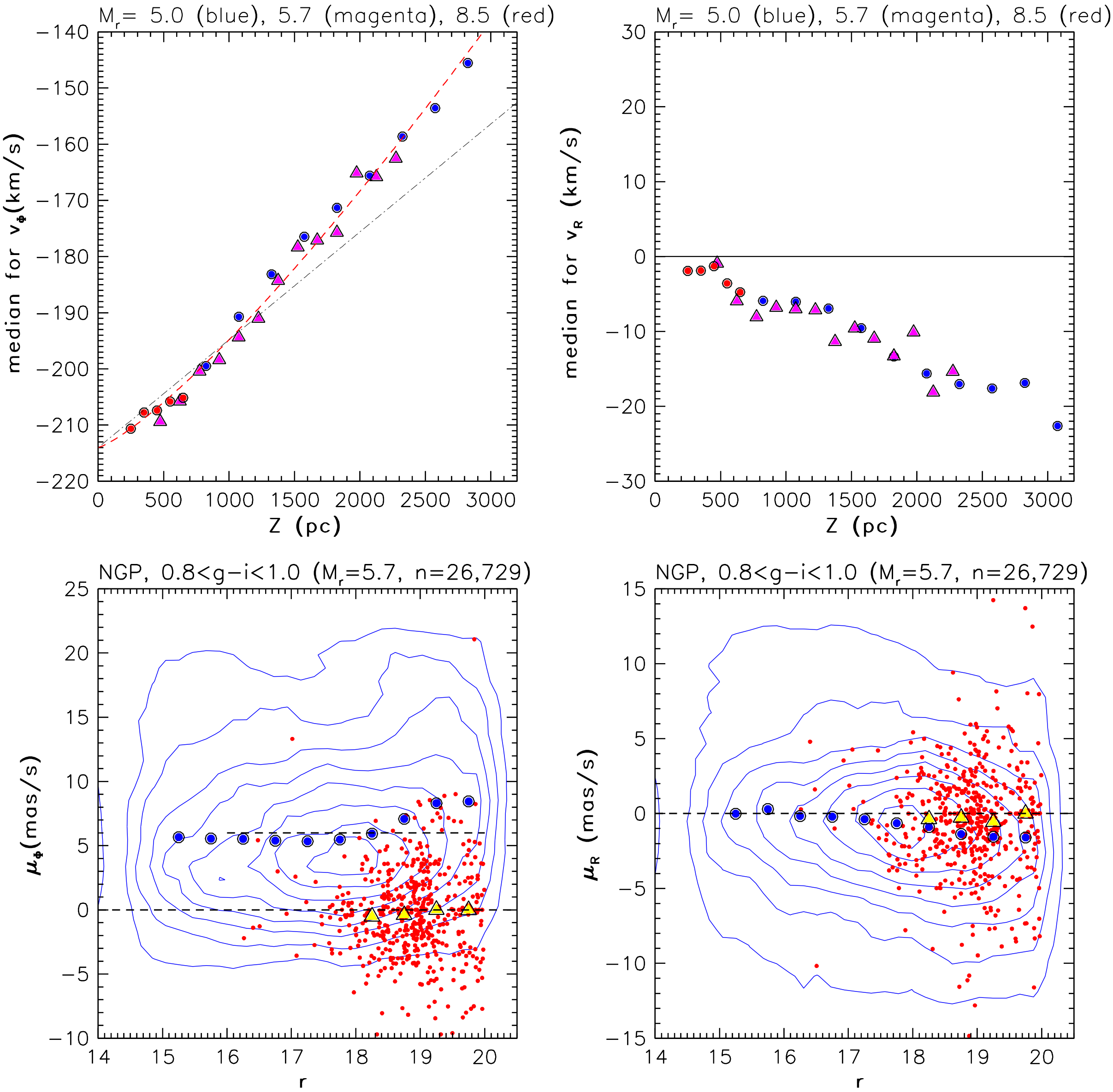

Fig. 9.— The top two panels show the dependence of the azimuthal (left) and radial (right) velocity component on distance from the galactic plane for three color-selected samples of disk stars whose M_r span 3.5 mag. The two lines in the top left panel show v_Φ = $(-214+19.2(Z/\mathrm{kpc})^k)$ km/s, for $k=1.0$ (lower, dot-dashed) and $k=1.25$ (dashed, upper). The bottom two panels display the corresponding proper motion components as a function of apparent magnitude for the sample shown as triangles in the top two panels ($M_r=5.7$). The distribution of individual measurements is shown as linearly spaced contours, with the binned medians shown by large blue dots. The small red dots are measurements for ∼500 quasars, and their medians are shown by large triangles. The non-linearity of the v_Φ vs. Z relation shown in the top left panel is seen in the bottom left panel as an upturn of median proper motion for $r>18$. This upturn is robust, as demonstrated by the quasar sample whose medians are consistent with zero. Similarly, the bottom right panel shows that the negative median radial velocity seen in the top right panel corresponds to a proper motion offset of ~ 1.5 mas/yr, which is not observed for the quasar sample.

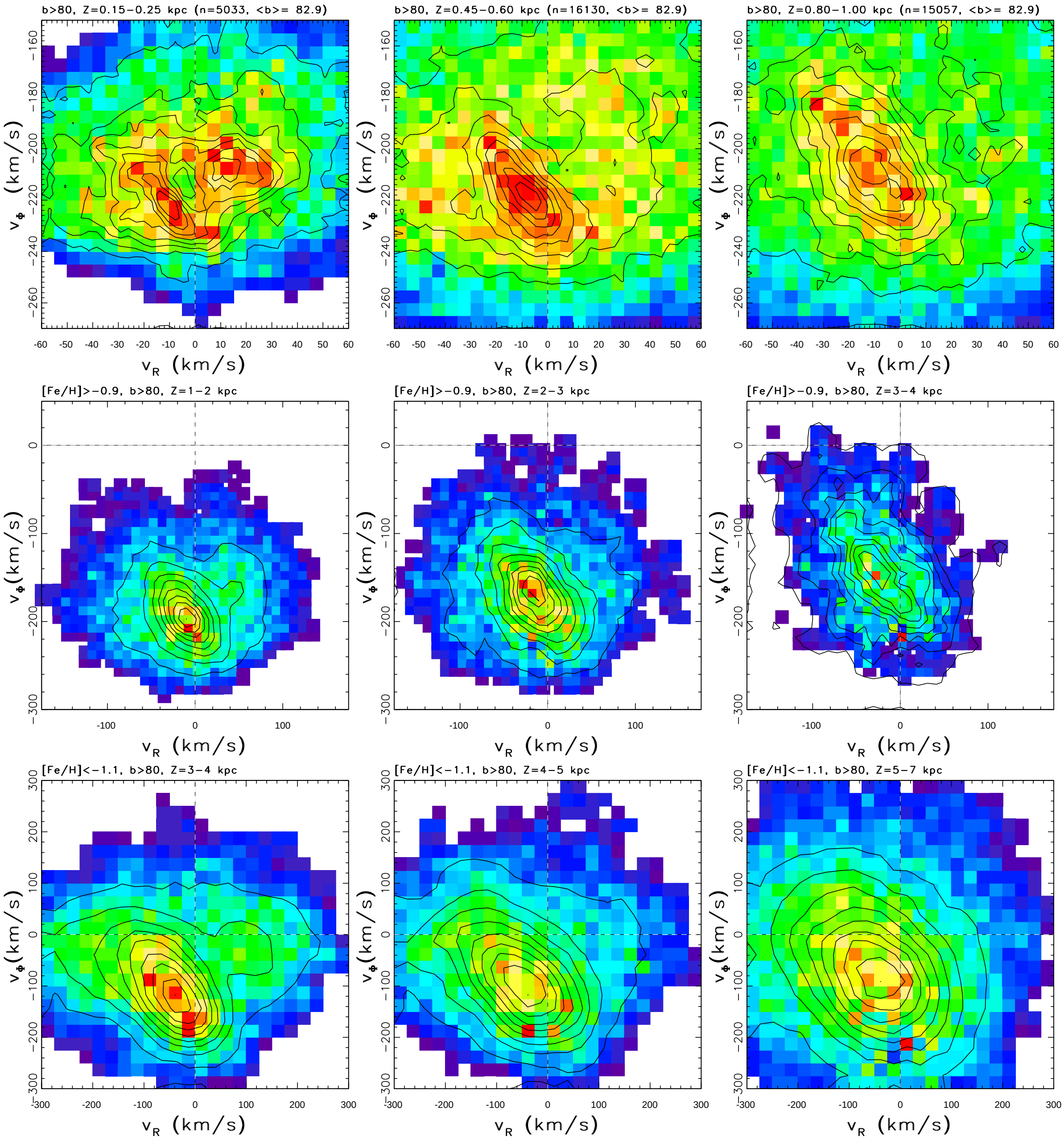

Fig. 10.— Each panel shows the v_Φ vs. v_R distribution for stars observed towards the North Galactic pole ($b > 80°$), and for a different range of the distance from the Galactic plane, Z. The counts in each bin are shown on a logarithmic scale (low to high: blue to green to red), and also as linearly spaced contours (obtained without binning). The top row shows the distributions for red stars ($g - i > 0.8$) and Z in the range 0.15-0.25 kpc, 0.45-0.60 kpc, and 0.80-1.0 kpc. The middle row shows high-metallicity (disk) F/G stars selected by $0.2 < g - r < 0.4$ and $[Fe/H] > -0.9$, and Z in the range 1-2 kpc, 2-3 kpc, and 3-4 kpc. The bottom row shows low-metallicity (halo) F/G stars selected by $0.2 < g - r < 0.4$ and $[Fe/H] < -1.1$, and Z in the range 3-4 kpc, 4-5 kpc, and 5-7 kpc. Note that each row has different velocity scales.

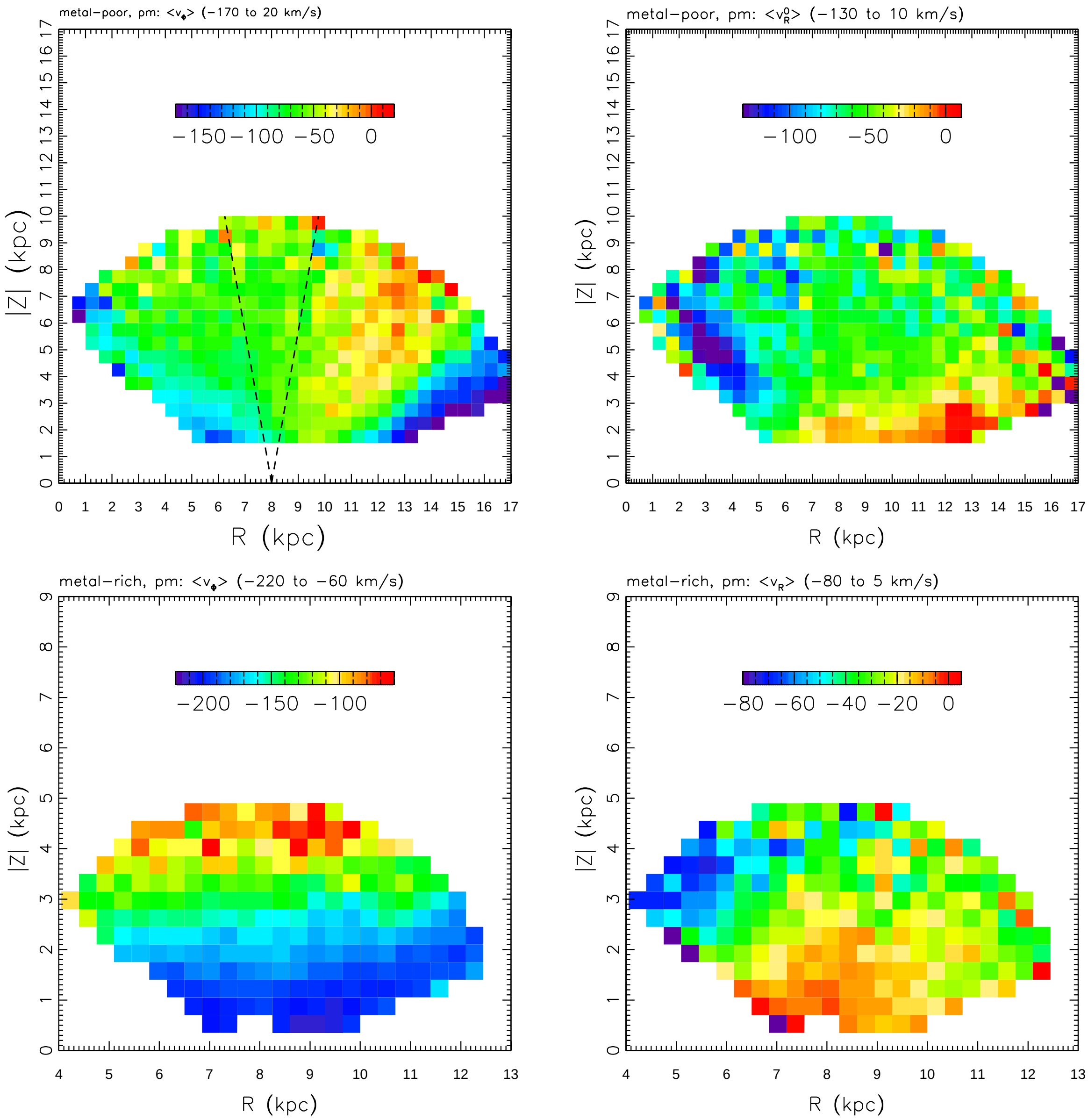

Fig. 11.— A comparison of the median v_Φ (determined from longitudinal proper motion, left panels) and v_R^0 (determined from latitudinal proper motion using the $v_Z = 0$ ansatz, right panels) velocity on galactocentric cylindrical coordinates, R and Z. The maps show results for subsamples of 176,250 low-metallicity ($[Fe/H] < -1.1$, top) and 119,719 high-metallicity ($[Fe/H] > -1.1$, top) F/G stars observed within 10° from the great circle defined by $l = 0°$ and $l = 180°$ (the prime meridian), or with $b > 80°$. Note that the spatial scale in the top panels is about twice as large as in the bottom panels. The dashed lines in the top left panel outline the region within 10° from the north galactic pole.

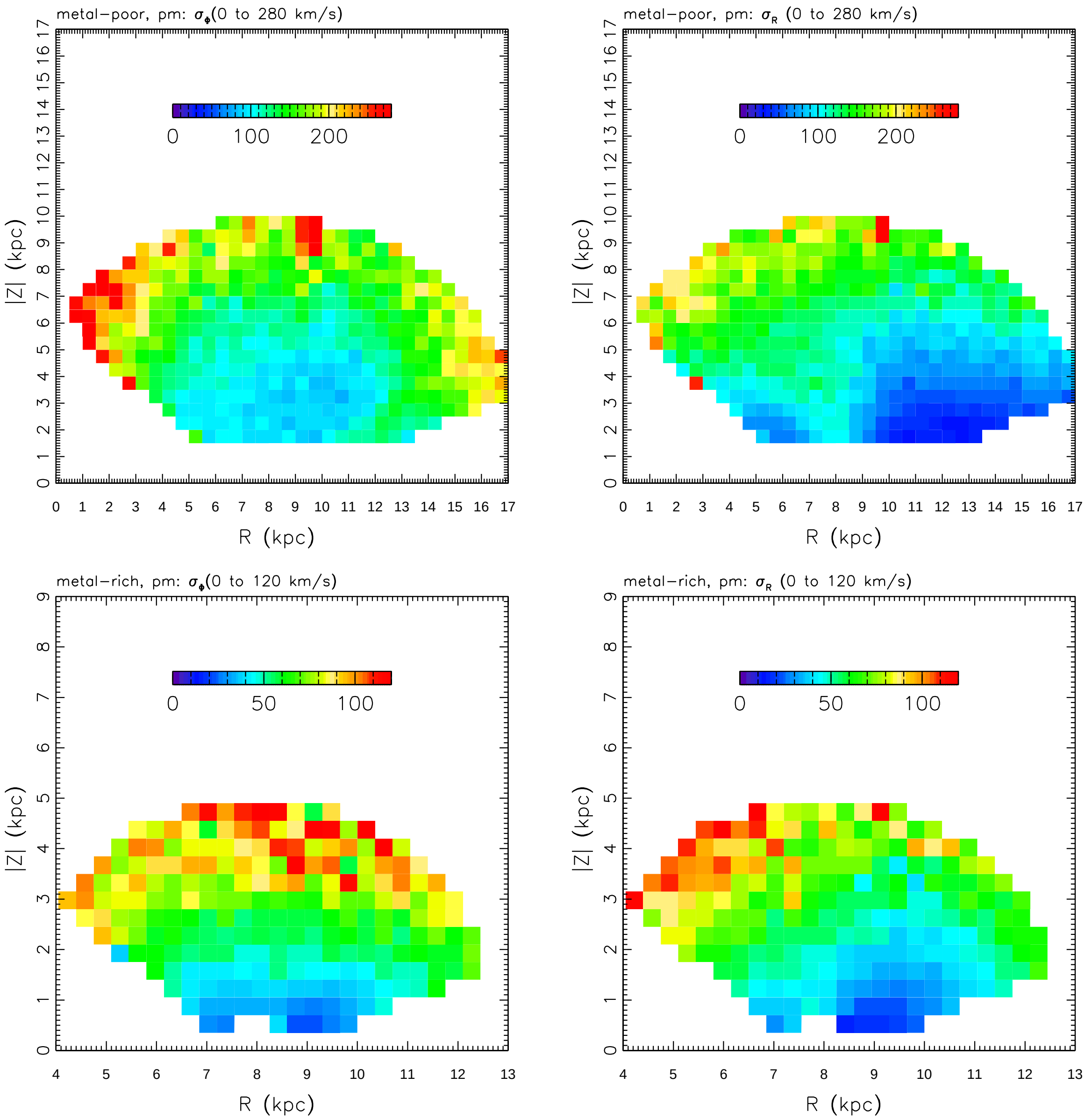

Fig. 12.— A comparison of the measured dispersion for v_Φ (determined from longitudinal proper motion, left panels) and v_{RZ} (determined from latitudinal proper motion, right panels) velocity on galactocentric cylindrical coordinates, R and Z, for the same metallicity-selected subsamples as shown in Figure 11 (note that here the v_{RZ} dispersion is shown, while the median for v_R^0 is shown in Figure 11, see text for clarification of this distinction). The contribution of measurement errors to velocity dispersion becomes non-negligible for large distances from (R=8,Z=0) kpc. Nevertheless, an increase of the v_Φ velocity dispersion with Z for high-metallicity stars (bottom left panel), and its increase as R decreases for low-metallicity stars (top left panel), is clearly discernible. Also, note that the v_{RZ} velocity dispersion increases as R decreases for both subsamples.

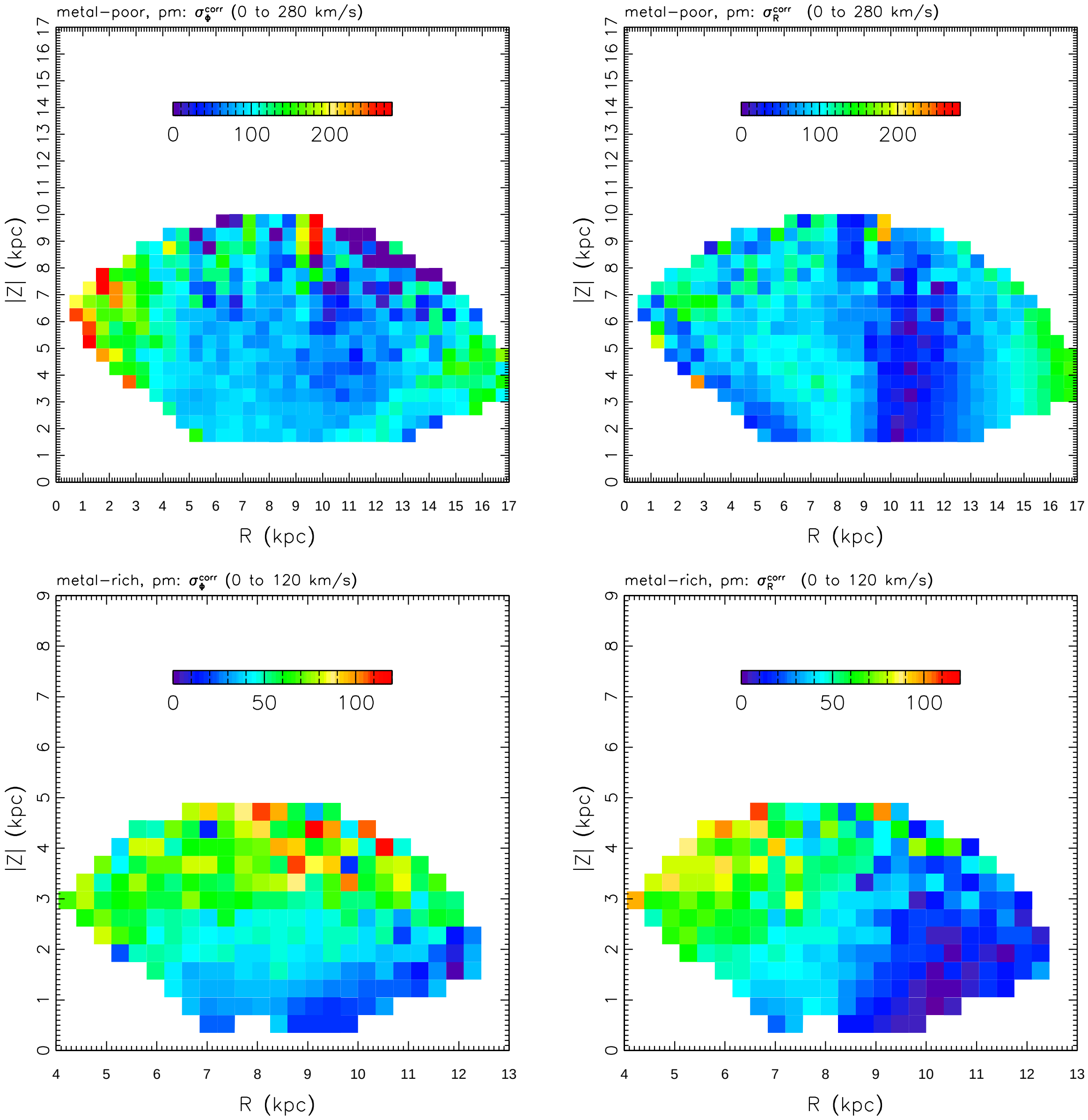

Fig. 13.— Analogous to Figure 12, except that the measured velocity dispersion is corrected by subtracting the measurement errors in quadrature. The top row corresponds to low-metallicity stars, and the bottom row to high-metallicity stars (note different spatial scales). The v_Φ dispersion is shown in the left column, and the v_{RZ} dispersion in the right column. Note that the color-coding of the velocity scale is the same as in Figure 12.

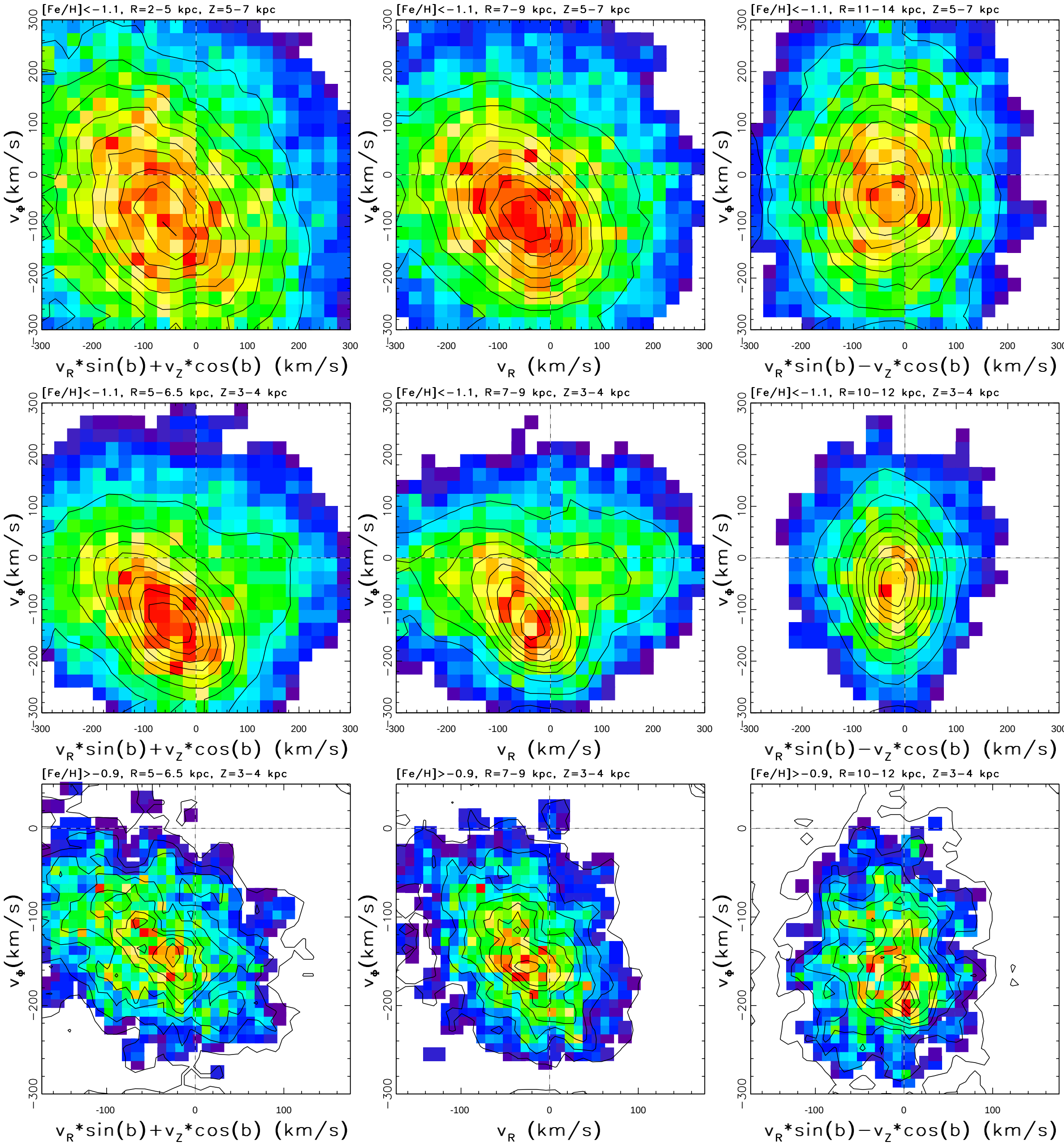

Fig. 14.— Each panel shows the v_Φ vs. v_{RZ} distribution for stars selected in narrow bins of R and Z, as indicated on top of each panel (compare to Figure 11). Here, v_{RZ} is short for a linear combination of v_R and v_Z velocity components, determined from latitudinal proper motion (see x axis labels and text). The counts in each bin are shown on a logarithmic scale (low to high: blue to green to red), and also as linearly spaced contours (obtained without binning). The top row shows low-metallicity stars ($[Fe/H] < -1.1$) with $5 < Z/\mathrm{kpc} < 7$, and with $2 < R/\mathrm{kpc} < 5$ (left panel), $7 < R/\mathrm{kpc} < 9$ (roughly towards the North Galactic pole, middle panel), and $11 < R/\mathrm{kpc} < 14$ (right panel). The middle row shows low-metallicity stars with $3 < Z/\mathrm{kpc} < 4$, and with $5 < R/\mathrm{kpc} < 6.5$ (left panel), $7 < R/\mathrm{kpc} < 9$ (middle panel), and $10 < R/\mathrm{kpc} < 12$ (right panel). Note that the strong correlation between v_Φ and v_R observed for $R < 9$ kpc, disappears for $R > 10$ kpc. The bottom panels show analogous $R - Z$ bins as in the middle row, except that high-metallicity stars ($[Fe/H] > -0.9$) are shown. They display similar behavior as low-metallicity stars.

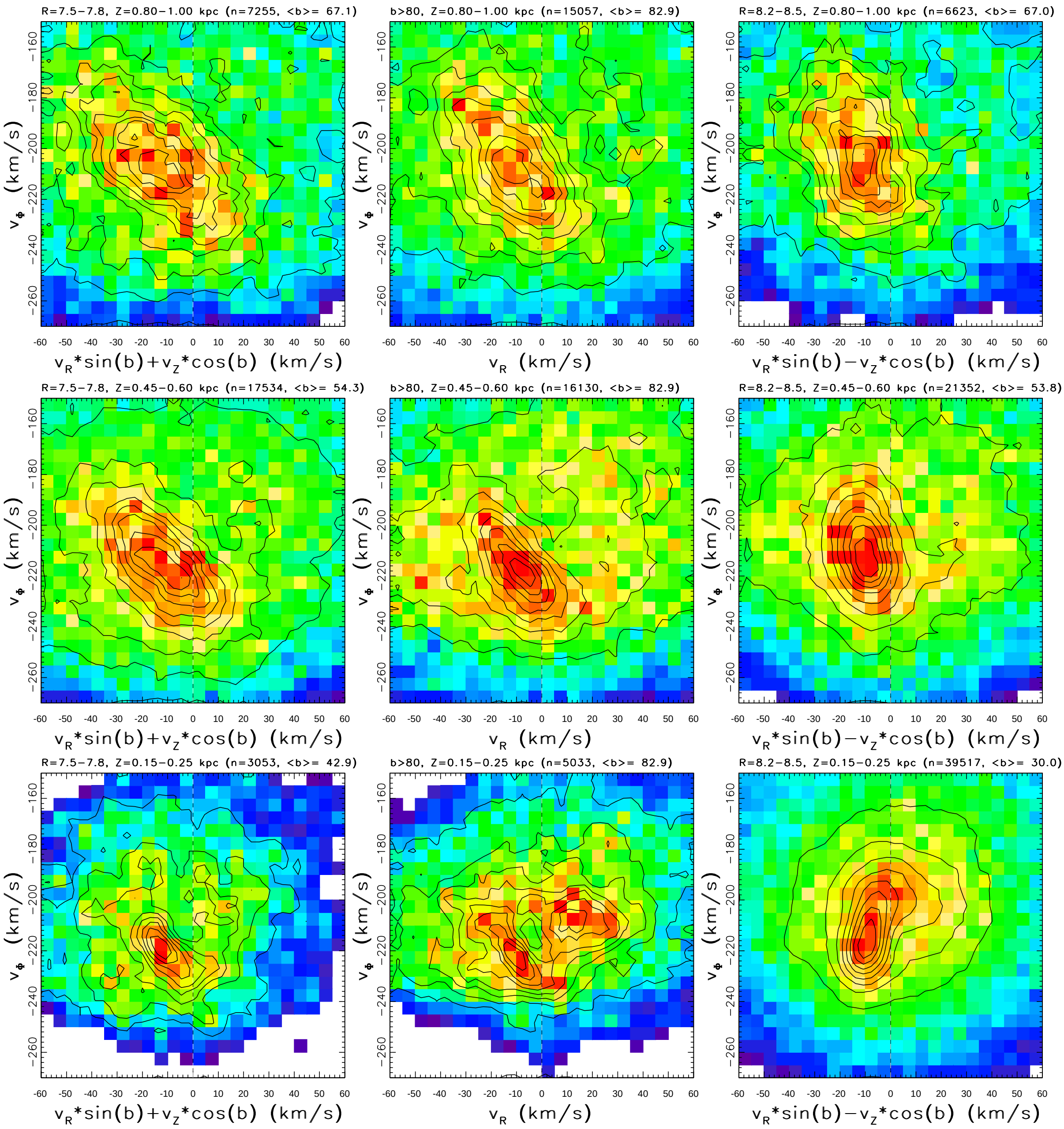

Fig. 15.— Similar to Figure 14, except that here only high-metallicity stars within a distance of 1 kpc are shown, and with $7.5 < R/\text{kpc} < 7.8$ (left column), $b > 80°$ (towards the North Galactic pole, middle column) and $8.2 < R/\text{kpc} < 8.2$, and distance from the Galactic plane, Z, of 0.15-0.25 kpc, 0.45-0.60 kpc, and 0.80-1.0 kpc, from the bottom to top row, respectively. The number of stars in each subsample and their median galactic latitude are also shown for each panel.

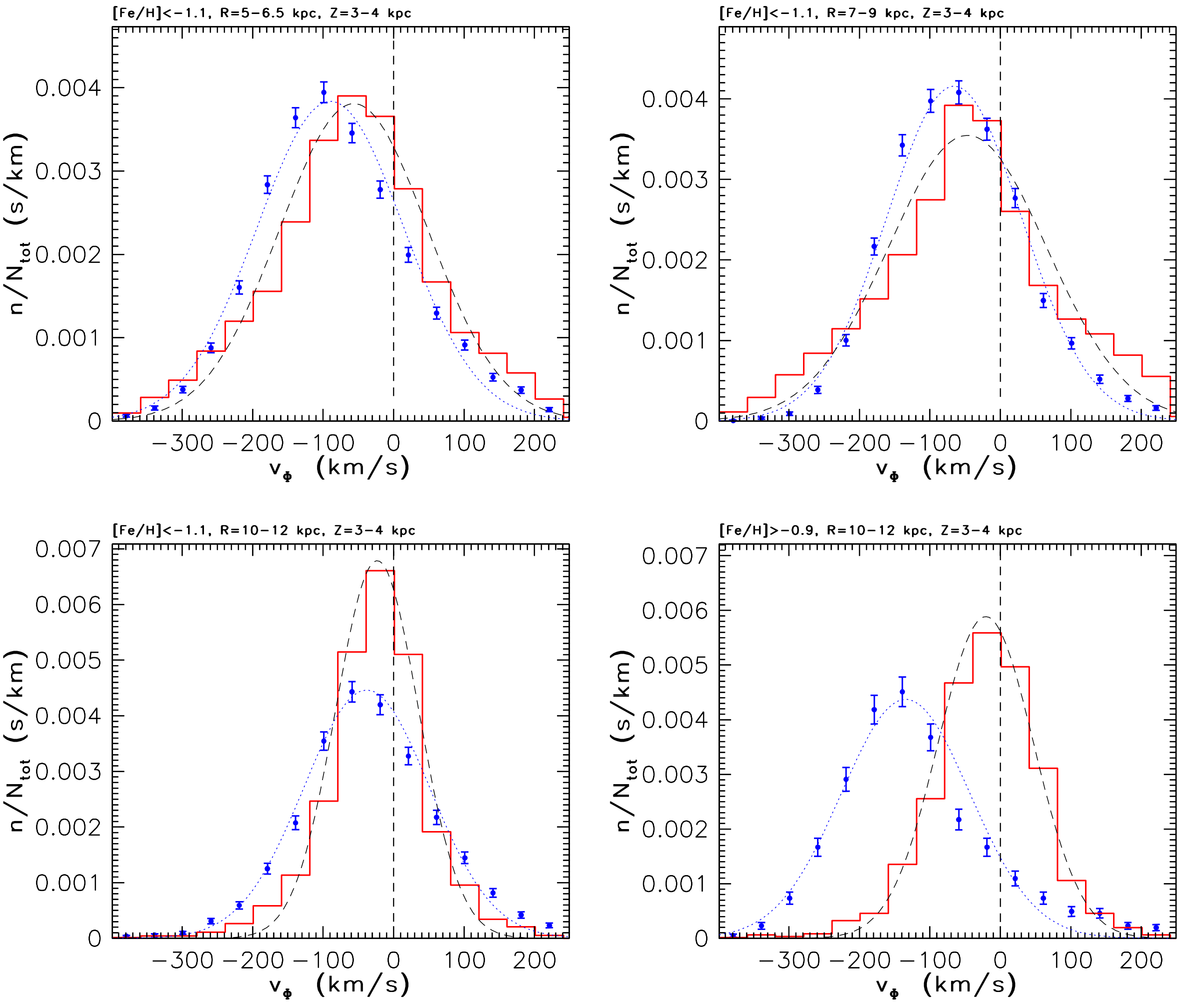

Fig. 16.— The v_Φ and v_{RZ} (see text for definition) distributions for samples of stars selected by metallicity and from small volumes defined by R and Z (Z=3–4 kpc, and R=5–6.5 kpc (top left), R=7–9 kpc (top right), and R=10–12 kpc (two bottom panels; low-metallicity left and high-metallicity right). The symbols with error bars show the v_Φ distributions, and histograms show the v_{RZ} distributions (errors are similar as for v_Φ). Note the large difference between the v_Φ distributions shown in the two bottom panels, and similarity of the v_{RZ} distributions. The best-fit Gaussians are shown by the dashed (v_{RZ}) and dotted (v_Φ) lines, with parameters listed in Table 1.

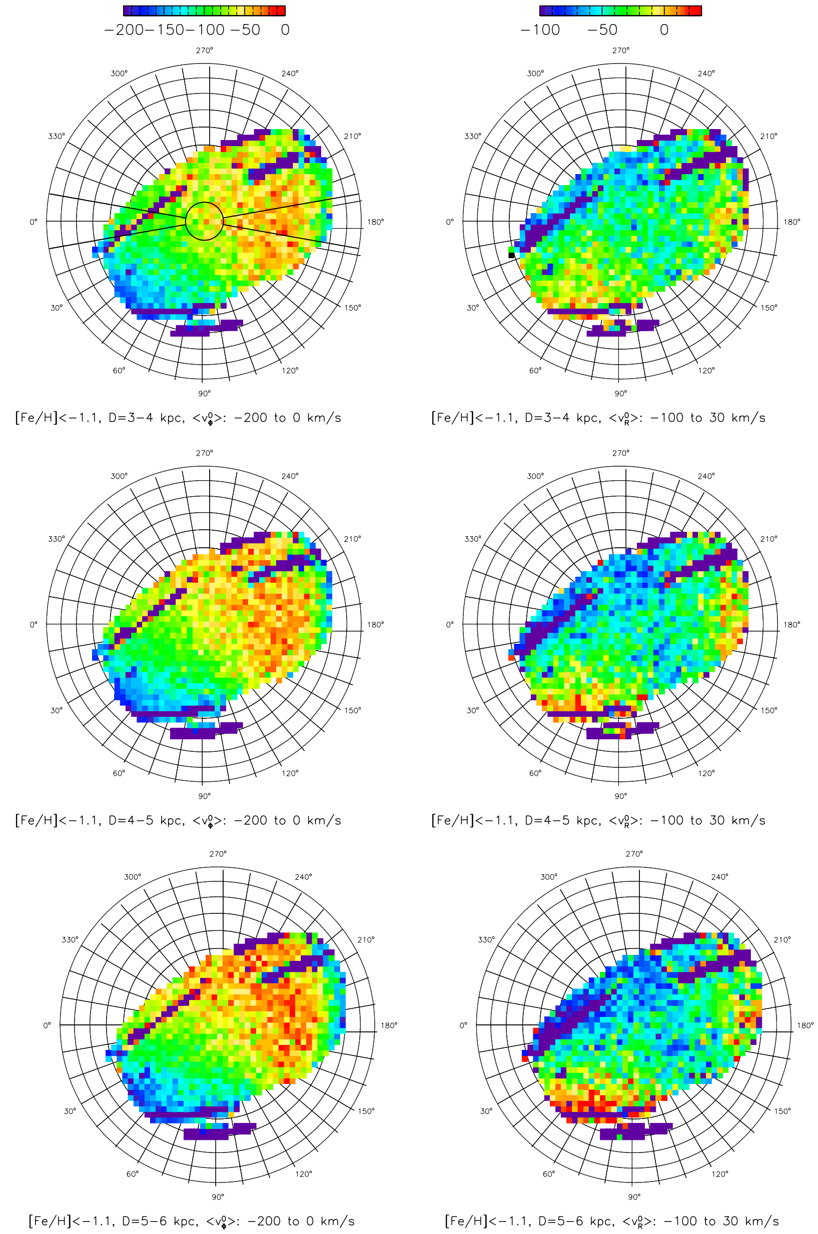

Fig. 17.— The dependence of the median v_Φ^0 (left) and v_R^0 (right) velocity components (derived from proper motion measurements using the $v_Z = 0$ ansatz) on galactic coordinates, for low-metallicity stars ($[Fe/H] < -1.1$) selected from three narrow distance ranges (top: 3–4 kpc, middle: 4–5 kpc, bottom: 5–6 kpc). The maps are shown in Lambert projection which preserves area (the north galactic pole is in the center, the outer circle corresponds to $b = 0°$, and the galactic center is towards left). The scale in linear, with the coded velocity range shown on top of each column (km/s). The small circle and four solid lines on top of the color-coded map in the top left panel outline the sky region used to select subsamples analyzed in Figure 11.

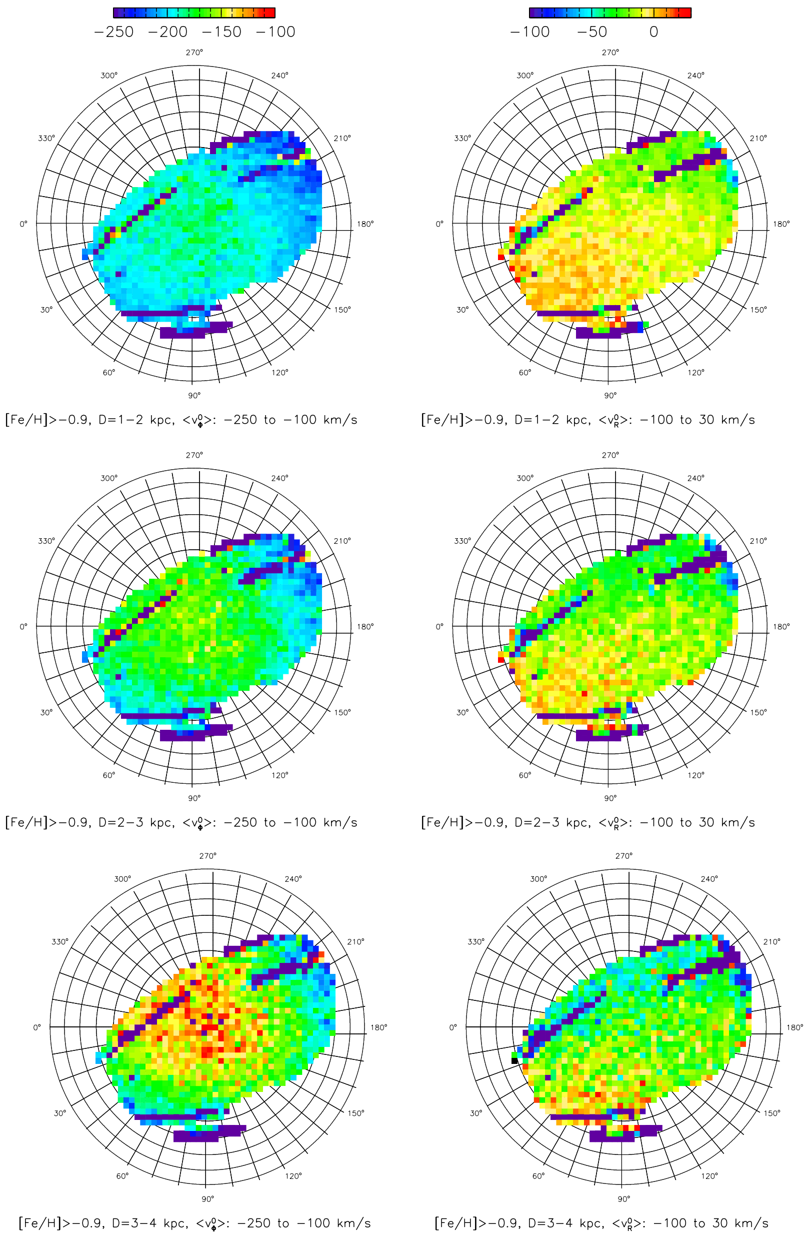

Fig. 18.— Analogous to Figure 25, except that data for high-metallicity stars ($[Fe/H] > -0.9$) are shown (top: 1–2 kpc, middle: 2–3 kpc, bottom: 3–4 kpc). The large coherent structure in the center of the bottom left panel (and to a smaller extent in other two panels in the left column) is due to vertical velocity gradient of the v_Φ component (compare to the bottom left panel in Figure 11).

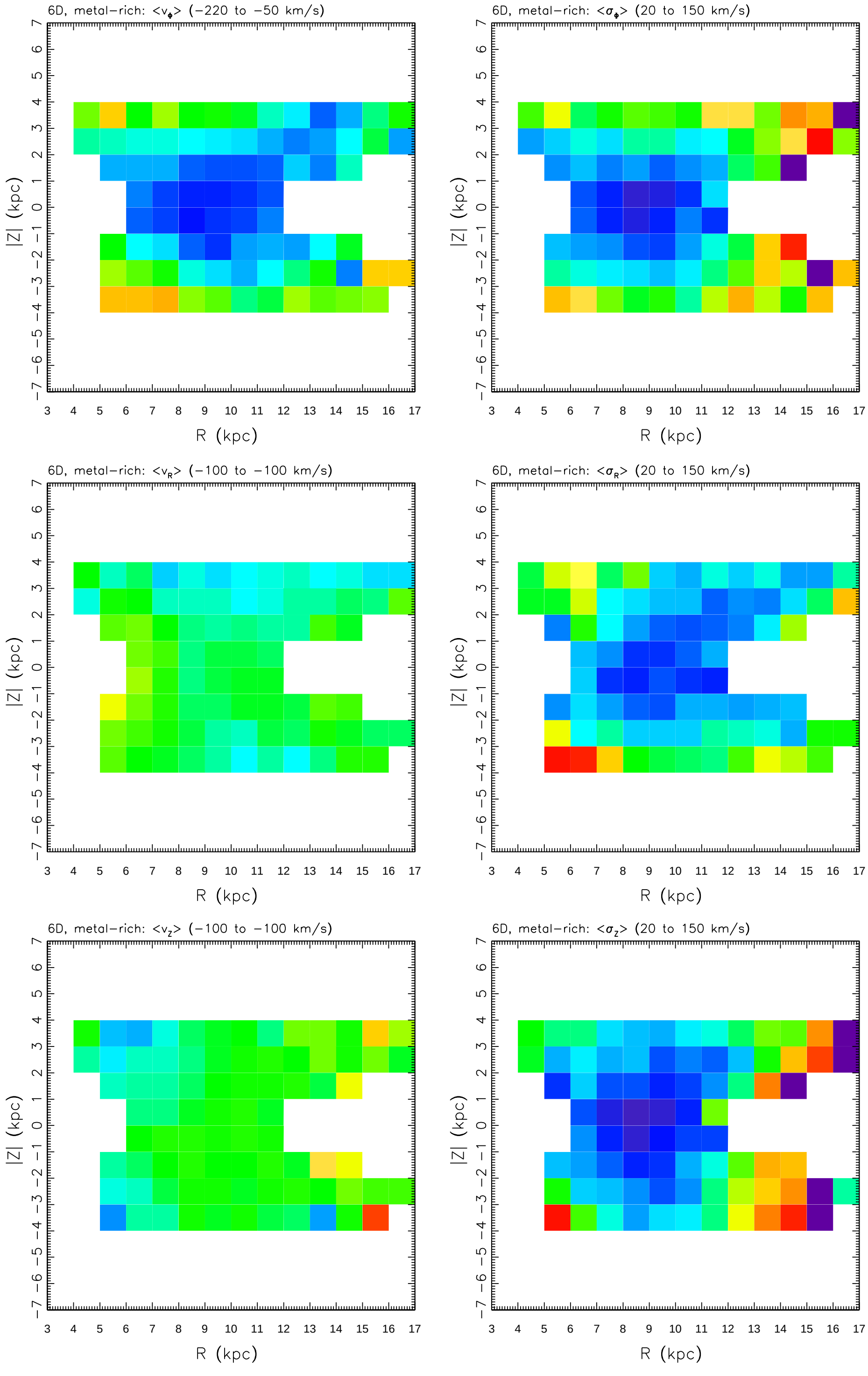

Fig. 19.— The dependence of the median velocity component (left column) and velocity dispersion (right column) for high-metallicity stars ($[Fe/H] > -1$) with radial velocity, with v_Φ in the top row, v_R in the middle row, and v_Z in the bottom row. In each pixel, stars from all azimuthal angles are included.

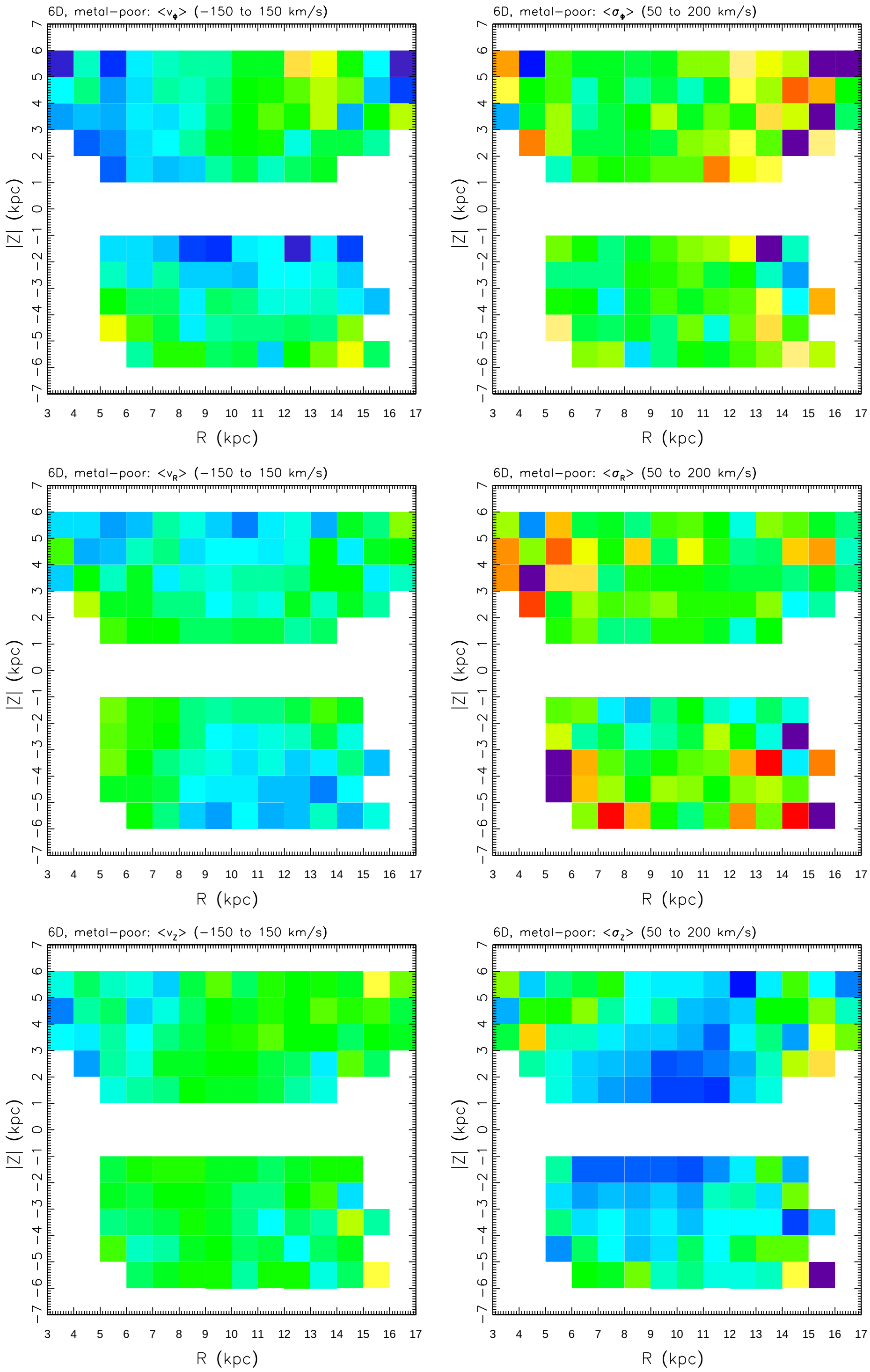

Fig. 20.— Analogous to Figure 19, except for low-metallicity stars ($[Fe/H] < -1$).

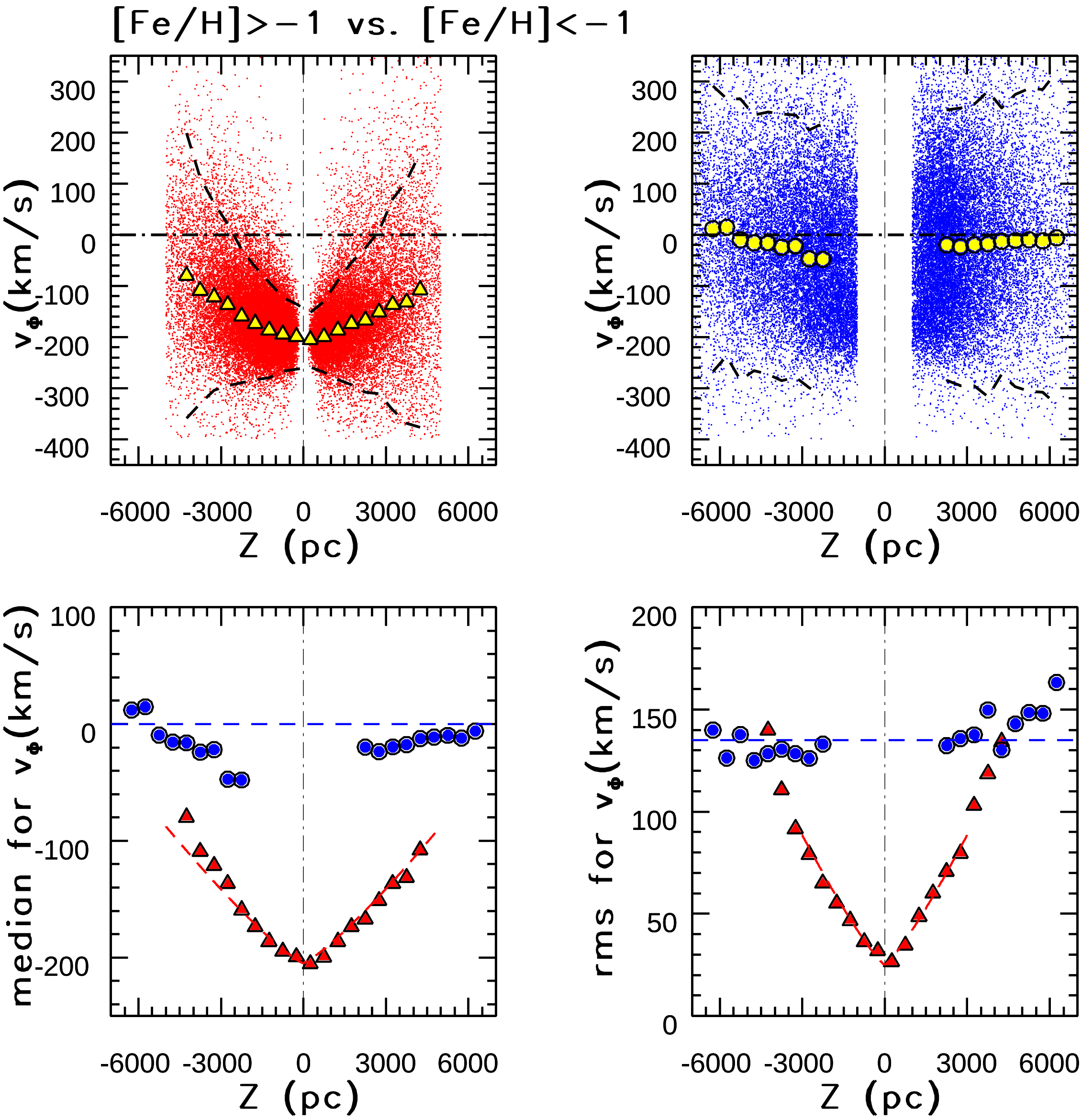

Fig. 21.— Analogous to Figure 7, except that here the sample includes stars with radial velocity, and all lines of sight, including the southern Galactic hemisphere ($Z < 0$).

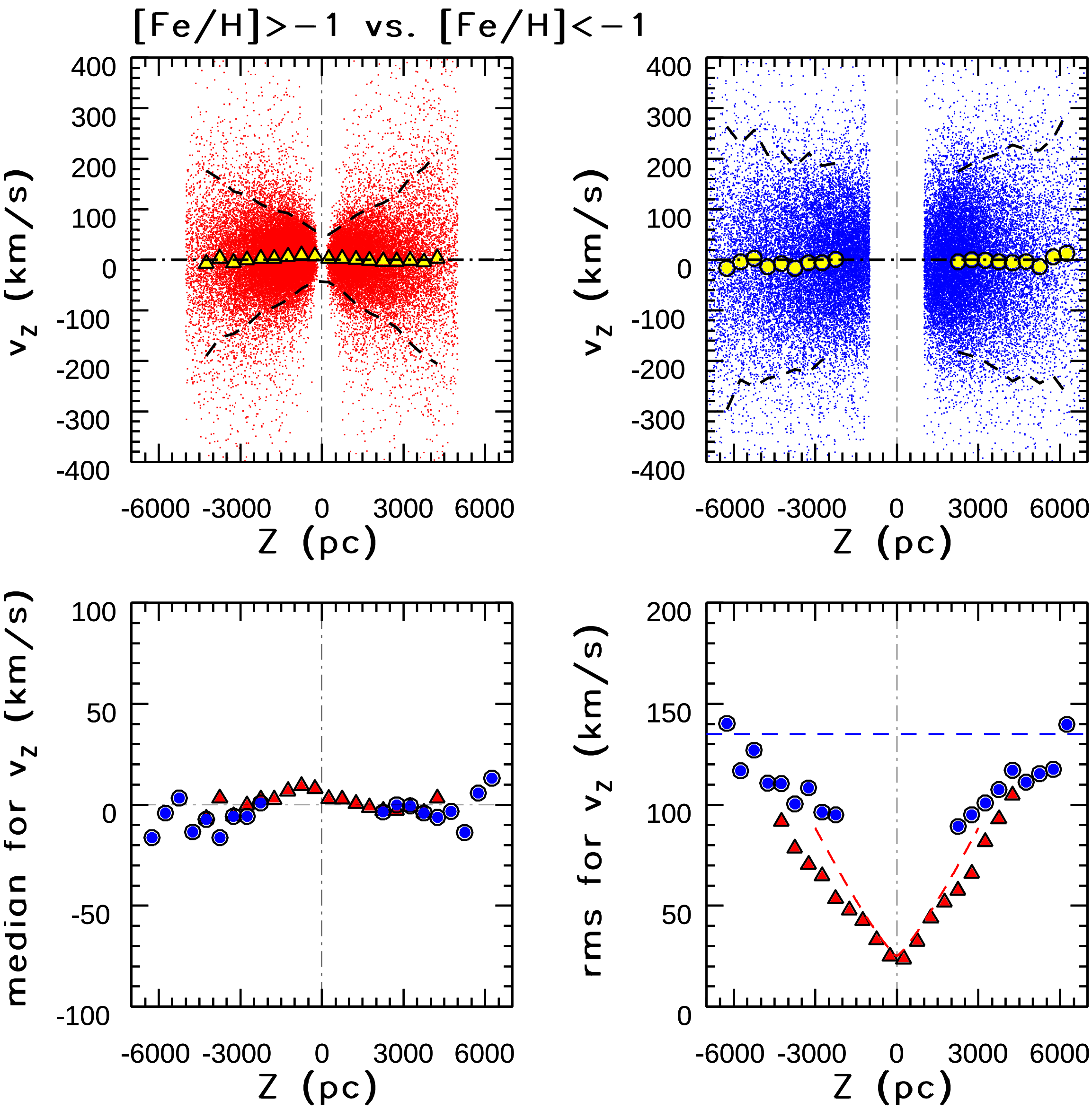

Fig. 22.— Analogous to Figure 21, except that here the v_Z component is shown.

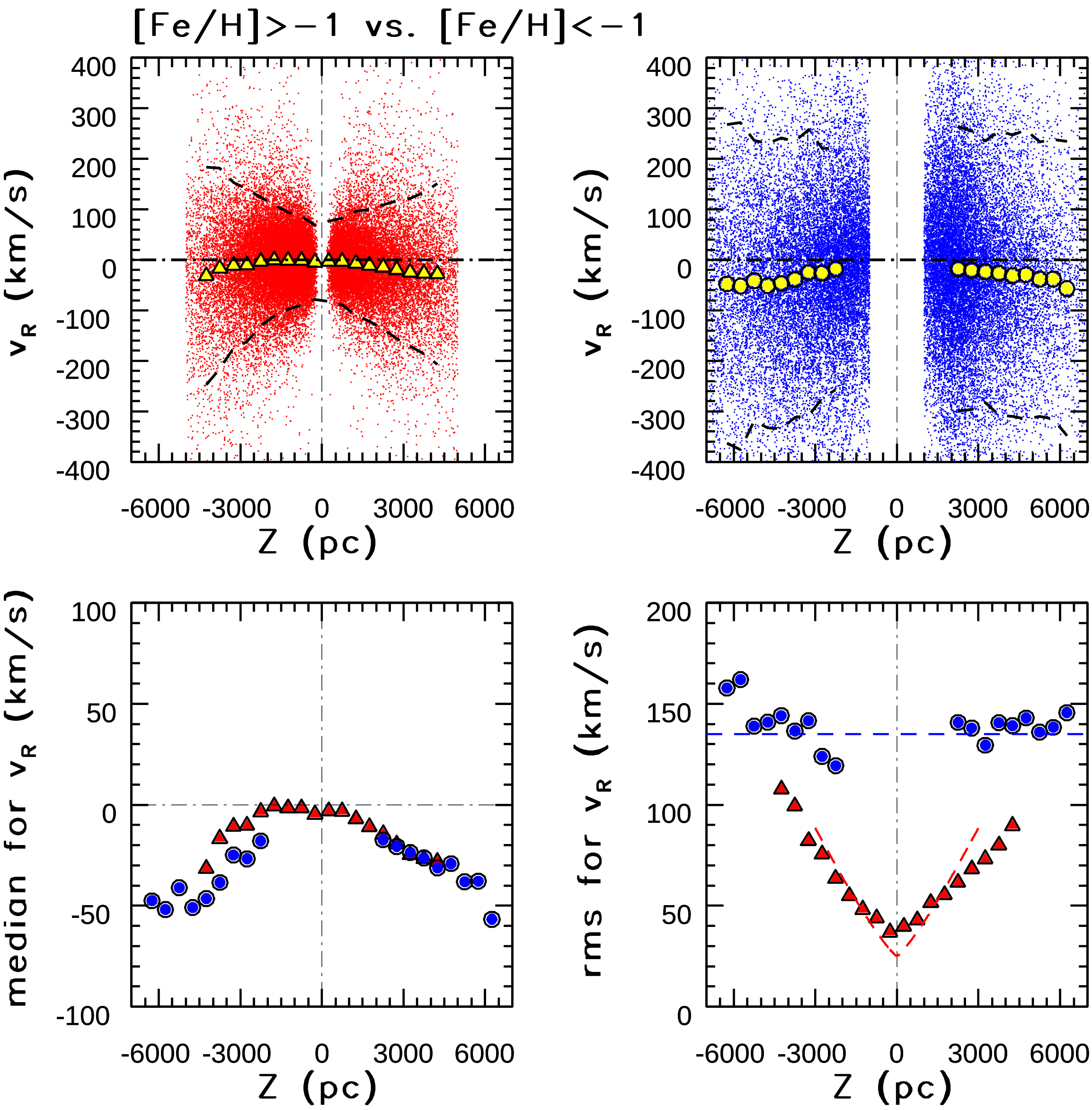

Fig. 23.— Analogous to Figure 21, except that here the v_R component is shown.

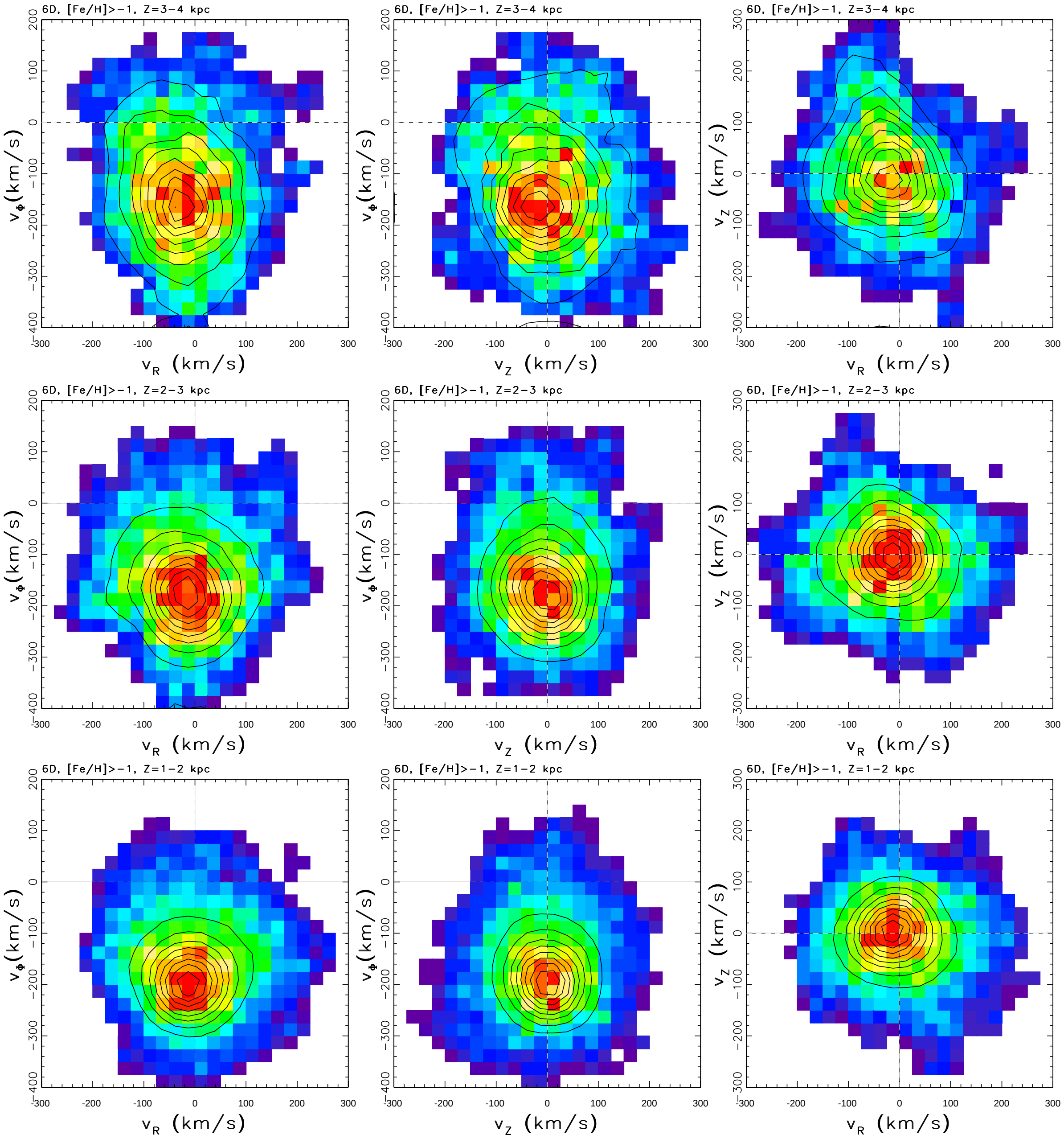

Fig. 24.— Each row shows the v_Φ vs. v_R, v_Φ vs. v_Z, and v_Z vs. v_R distributions for high-metallicity (disk) F/G stars selected by $0.2 < g - r < 0.4$ and $[Fe/H] > -1.$ and Z in the range 1-2 kpc (bottom), 2-3 kpc (middle), and 3-4 kpc (top). The counts in each bin are shown on a logarithmic scale (low to high: blue to green to red), and also as linearly spaced contours (obtained without binning).

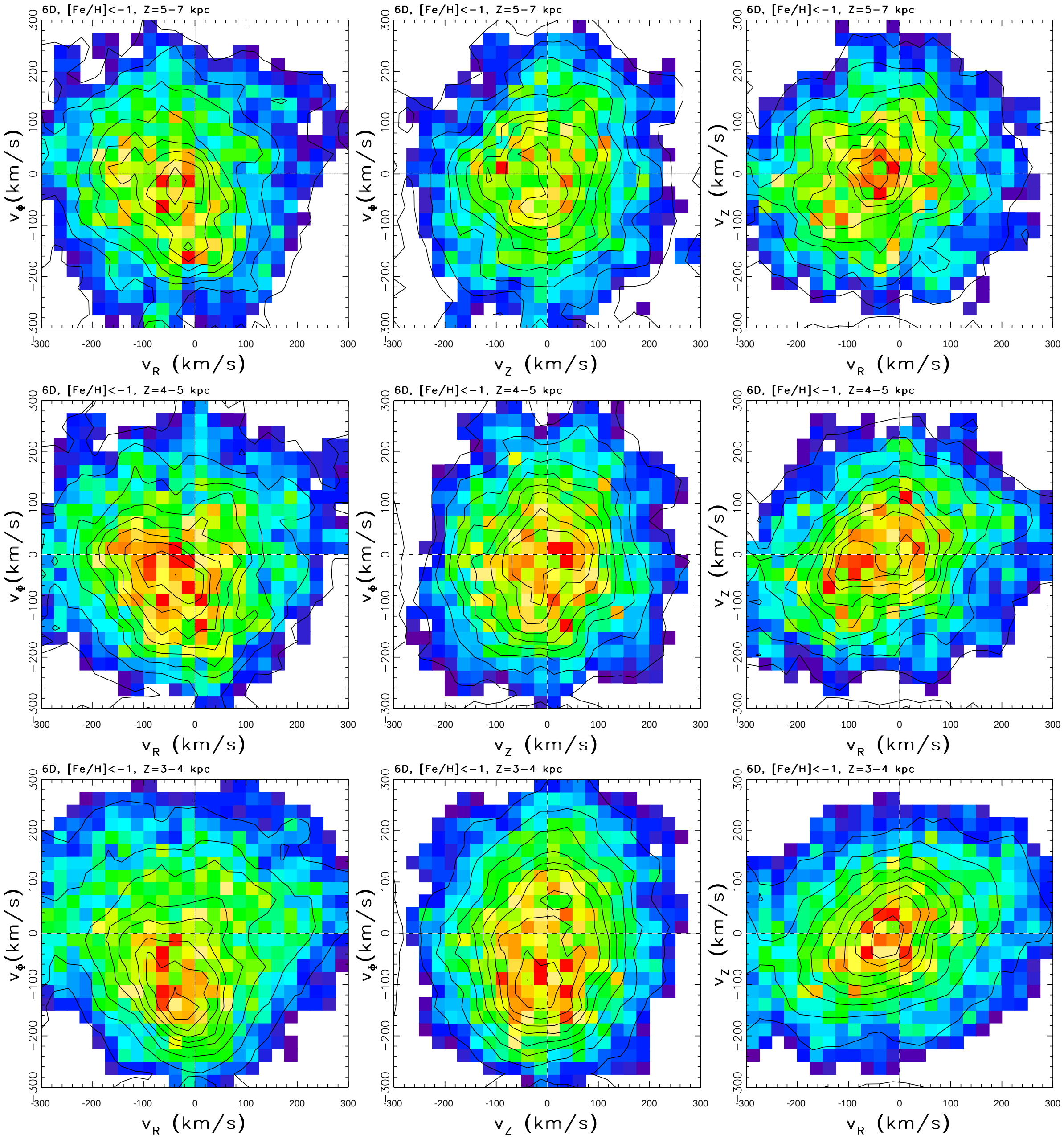

Fig. 25.— Analogous to Figure 24, except that the velocity distributions are shown for low-metallicity (halo) F/G stars selected by $0.2 < g - r < 0.4$ and $[Fe/H] < -1$, and Z in the range 3-4 kpc, 4-5 kpc, and 5-7 kpc. Note that the v_Z vs. v_R velocity ellipsoid (right column) approximately points towards the Galactic center in all three Z bins.

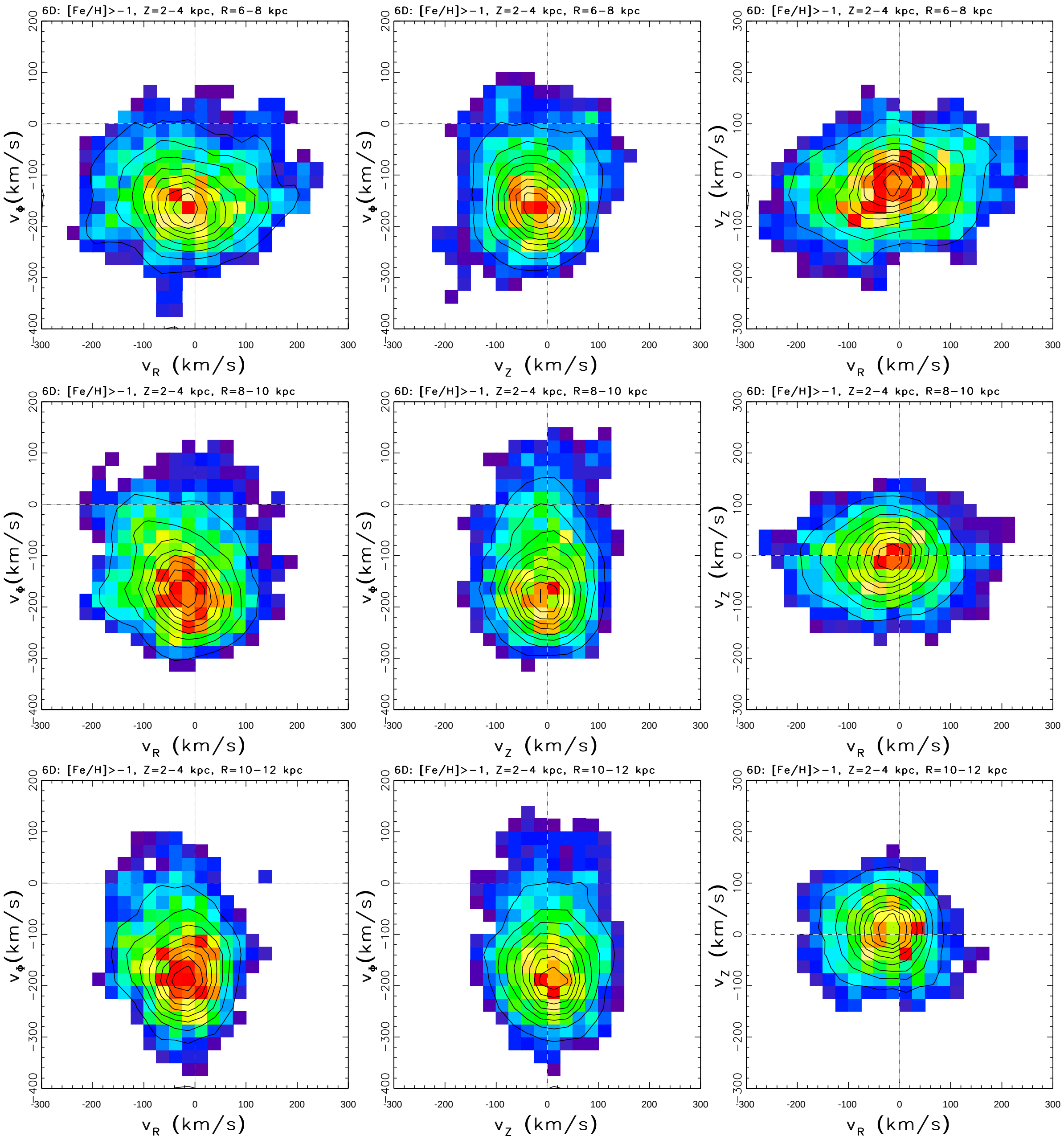

Fig. 26.— Analogous to Figure 24, except that the velocity distributions are shown for a constant range of $Z = 2 - 4$ kpc, and for R in the range 6-8 kpc (top row), 8-10 kpc (middle row) and 10-12 kpc (bottom row).

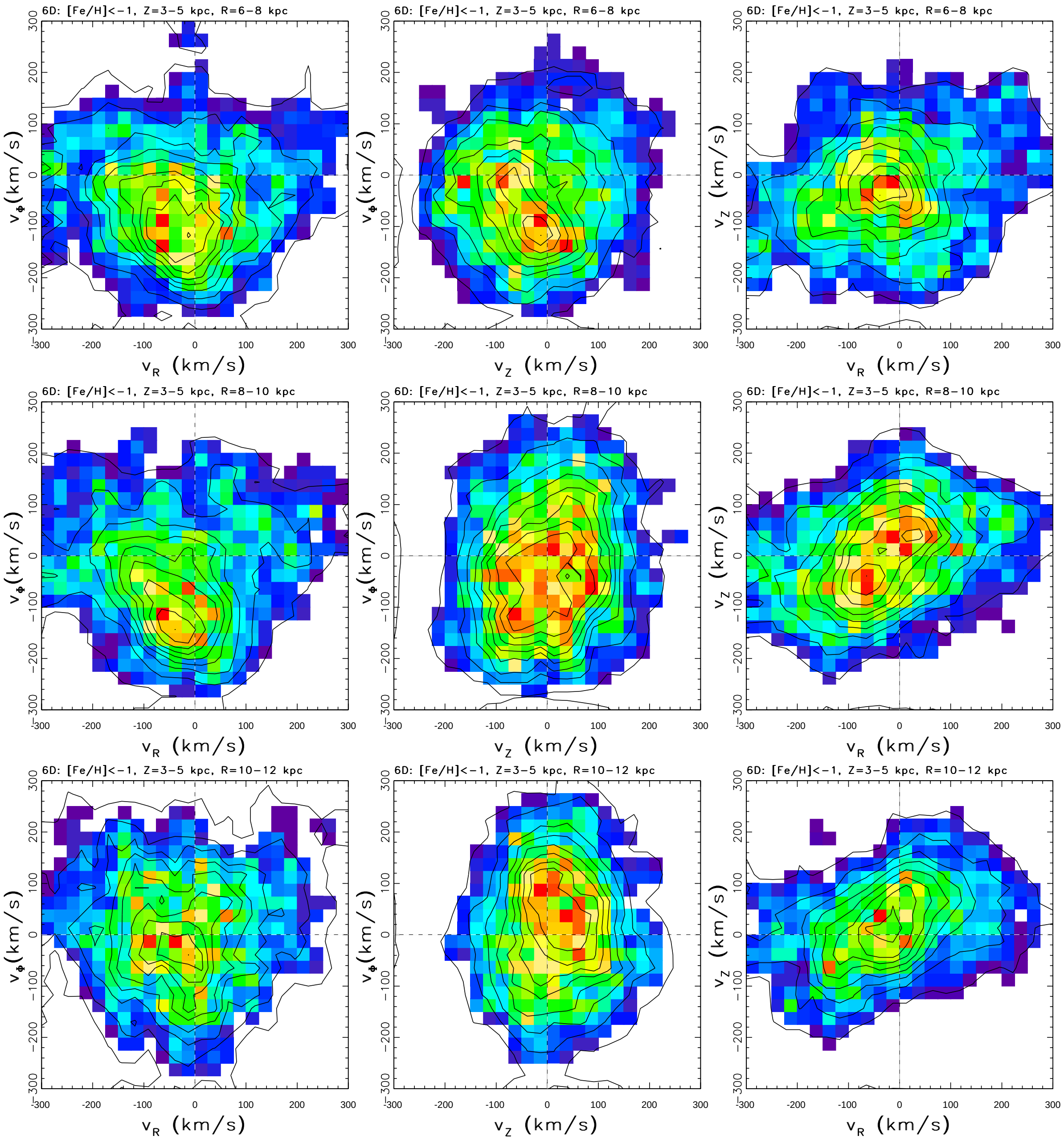

Fig. 27.— Analogous to Figure 25, except that the velocity distributions are shown for a constant range of $Z = 3-5$ kpc, and for R in the range 6-8 kpc (top row), 8-10 kpc (middle row) and 10-12 kpc (bottom row).

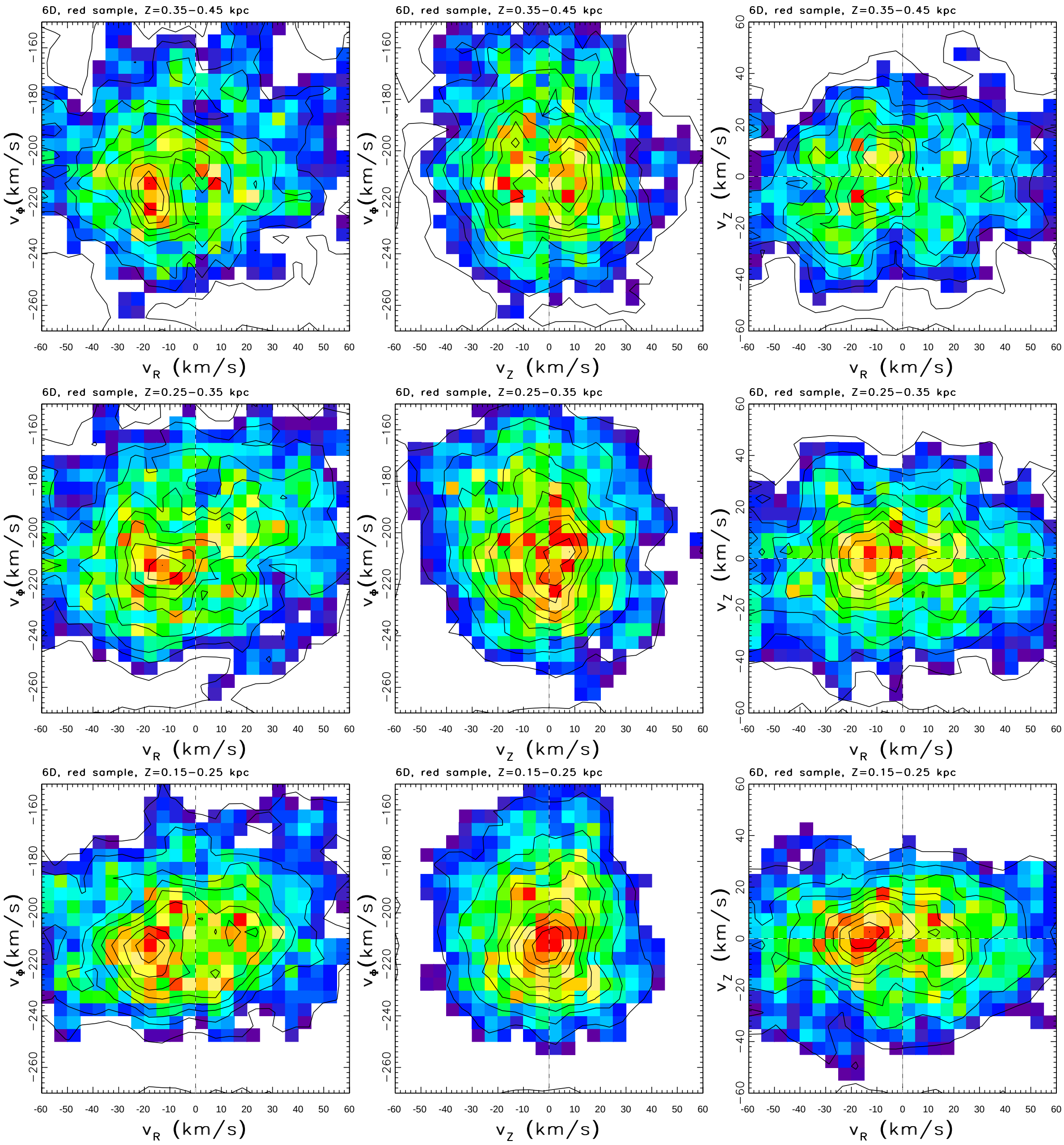

Fig. 28.— Analogous to Figure 24, except that the velocity distributions are shown for red stars ($g - i > 0.8$) and Z in the range 0.15-0.25 kpc, 0.25-0.35 kpc, and 0.35-0.45 kpc, from the bottom to top row, respectively.

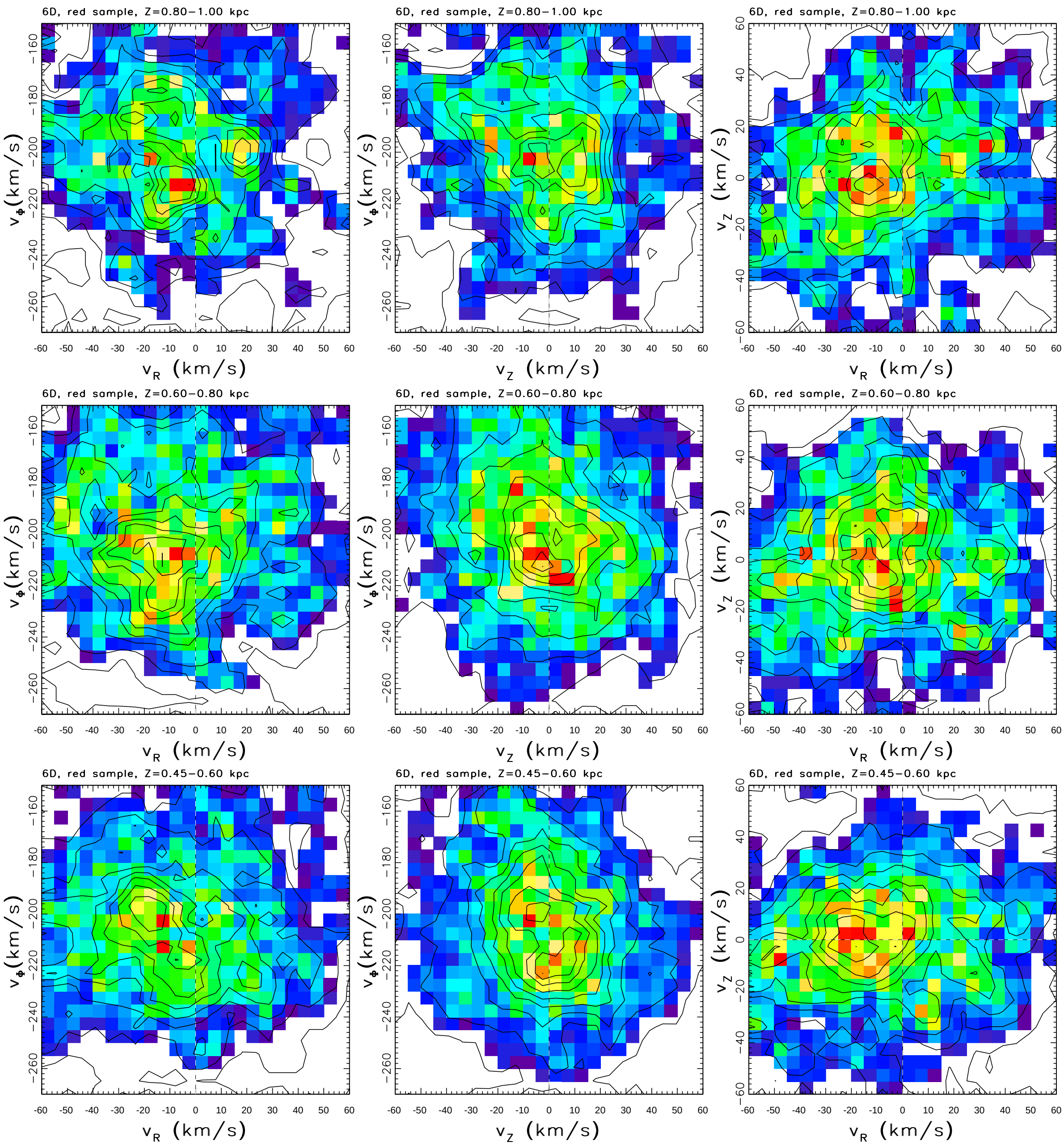

Fig. 29.— Analogous to Figure 28, except that the Z bins are 0.45-0.60 kpc, 0.60-0.80 kpc, and 0.80-1.0 kpc, from the bottom to top row, respectively.

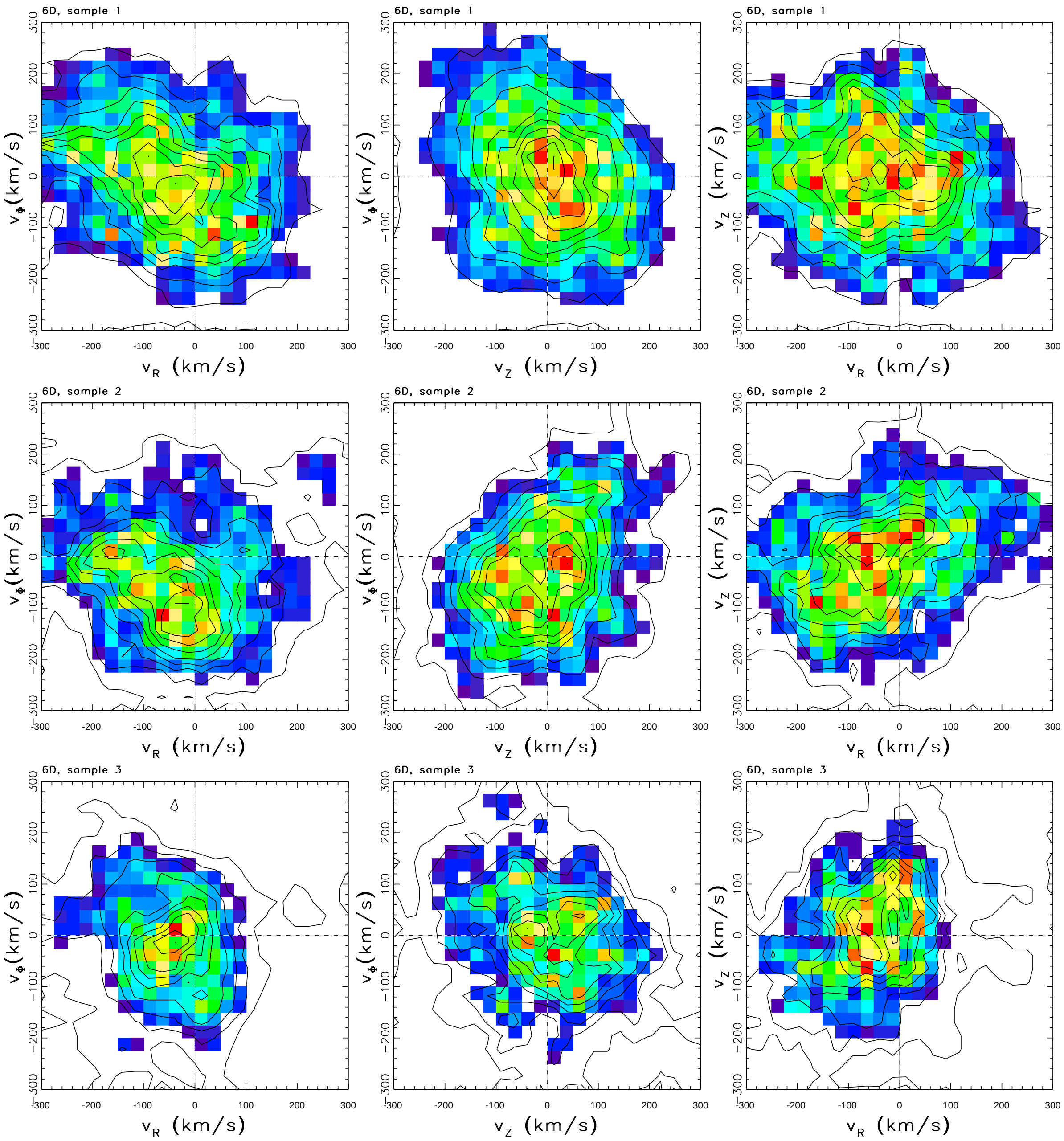

Fig. 30.— Analogous to Figure 25, except that three control samples of low-metallicity stars are selected from roughly the same R and $|Z|$ range, but with different azimuthal angles, using cuts in galactic coordinates (see Table X). The top row corresponds to $R \sim 9$ kpc and $Z \sim -5$ kpc ($l \sim 110°$, $b \sim -61°$), the middle row to $R \sim 9$ kpc and $Z \sim 5$ kpc ($l \sim 100°$, $b \sim 60°$), and the bottom row to $R \sim 8$ kpc and $Z \sim 5$ kpc ($l \sim 270°$, $b \sim 60°$).